NASA TECHNICAL MEMORANDUM

NASA TM X-1243

NASA TM X-1243

TM X- 1243

THE EFFECT OF PROTUBERANCES, CAVITIES, AND ANGLE OF ATTACK ON THE WIND-TUNNEL PRESSURE AND HEAT-TRANSFER DISTRIBUTION FOR THE APOLLO COMMAND MODULE

by John J. Bertin

Manned Spacecraft Center

Houston, Texas

NATIONAL AERONAUTICS AND SPACE ADMINISTRATION • WASHINGTON, D. C. • OCTOBER 1966

NASA TM X-1243

THE EFFECT OF PROTUBERANCES, CAVITIES, AND ANGLE OF ATTACK ON THE WIND-TUNNEL PRESSURE AND HEAT-TRANSFER DISTRIBUTION FOR THE APOLLO COMMAND MODULE

By John J. Bertin

Manned Spacecraft Center
Houston, Texas

NATIONAL AERONAUTICS AND SPACE ADMINISTRATION

For sale by the Clearinghouse for Federal Scientific and Technical Information
Springfield, Virginia 22151 – Price $2.50

THE EFFECT OF PROTUBERANCES, CAVITIES, AND ANGLE OF ATTACK ON THE WIND-TUNNEL PRESSURE AND HEAT-TRANSFER DISTRIBUTION FOR THE APOLLO COMMAND MODULE

By John J. Bertin
Manned Spacecraft Center

SUMMARY

Heat-transfer-rate and pressure distributions obtained in wind tunnels for the Apollo command module having neither cavities nor protuberances are presented for angles of attack from 0° to 33°. The wind tunnel conditions include free-stream Mach numbers from 6 to 10, with Reynolds numbers from 0.17×10^6 to 1.2×10^6, based on the free-stream fluid properties and the maximum body diameter of the model. The measured heating-rate and pressure distributions are compared with theoretical distributions. In the pitch plane of the spherical heat shield, modified Newtonian pressures approximate the measured values (except near the stagnation point and near the toroidal section), while the experimental heating rates are between the values calculated for two-dimensional flow and axisymmetric flow.

Also presented are data illustrating the effect on the heat transfer to the Apollo reentry configuration of cavities and protuberances. The measurements were made at a free-stream Mach number of 10 for Reynolds numbers from 1.37×10^6 to 2.56×10^6. The data indicate significant increases in the heat-transfer rate over large regions of the command module, due to the presence of protuberances and cavities.

INTRODUCTION

Estimates of the cold-wall, nonblowing convective heat-transfer rates for the Apollo reentry configuration are based on wind-tunnel measurements. Reference 1 presents, in detail, pressure and heat-transfer-rate data at

angles of attack of 0° and 33° for an Apollo reentry configuration having neither cavities nor protuberances (referred to in this report as the "clean configuration"). References 2 to 5 report heat-transfer and pressure measurements for the clean configuration over a wide range of angle of attack. In order to predict local heating rates on the reentry configuration, it is necessary to include perturbations due to the presence of windows, antennae, and other surface modifications. Reference 6 presents interference heat-transfer data obtained at an angle of attack of 33°.

The present paper provides clean configuration heat-transfer and pressure measurements at angles of attack from 0° to 33°. The data, which were obtained in Tunnel C at Arnold Engineering and Development Center (AEDC) and in the 21-in. hypersonic wind tunnel (HWT) at the Jet Propulsion Laboratory (JPL) are compared with theory. In addition, wind tunnel heat-transfer rates are given which illustrate the effects of cavities and protuberances over an angle-of-attack range of 18° to 37°.

NOMENCLATURE

h	enthalpy
k	thermal conductivity of air
M	Mach number
N_{Pr}	Prandtl number
p	pressure
$\dot{q}$	local heat-transfer rate
$\dot{q}_{ihf}$	ratio of the heat-transfer rate measured with interference to the heat-transfer rate measured at the same location on a clean command module, also referred to as the interference heating factor
$\dot{q}_{t)\alpha=0°}$	heat-transfer rate at the zero angle-of-attack stagnation point
R	maximum body radius, 77 inches for full-scale command module

Re_D	Reynolds number, based on free-stream fluid properties and maximum body diameter, also referred to as free-stream Reynolds number
Re_x	Reynolds number, based on local fluid properties and distance along the surface from stagnation point
r_o	radius of cross section of body of revolution
S	distance along surface from geometric center of spherical heat shield
S_c	distance along surface from geometric center to maximum body radius
T	absolute temperature
V	velocity
x	distance along the surface from the stagnation point
α	angle of attack; for zero angle of attack the axis of symmetry is parallel to the free-stream flow with the spherical heat shield forward
θ	angle between a normal to surface and direction free-stream flow
λ	angle between windward half of pitch plane and the instrumentation place
μ	viscosity
ρ	density

Subscripts:

aw	conditions assuming an adiabatic wall
l	local conditions external to boundary layer
t	conditions at stagnation point of body

w conditions at wall

∞ free-stream conditions

Superscripts:

* properties are evaluated using Eckert's reference temperature

FACILITIES AND MODELS

The measurements presented in this report were made either in the 21-in. HWT at the JPL or in Tunnel C at AEDC. The 21-in. HWT is a continuous-flow tunnel using a flexible, two-dimensional nozzle to provide a choice of test-section Mach numbers from 4 to 11. Tunnel C is a continuous-flow tunnel in which air is expanded through a fixed conical nozzle to a nominal free-stream Mach number of 10.

A sketch of the 0.02 scale model used in the 21-in. HWT is shown in figure 1(a). The model was supported by a circular sting, 0.75 in. in diameter, which made an angle of 28° with the axis of symmetry. The model was constructed of 310 stainless steel with a nominal skin thickness of 0.030 in. Iron-constantan thermocouples were fusion-welded to the inner surface to obtain the temperature histories necessary to determine the heat-transfer rates.

Figure 1(b) presents a sketch of the 0.045-scale Apollo model used in Tunnel C. The support sting made an angle of 9° with the axis of symmetry. Just prior to entering the model, the sting had a circular cross-section 1.25 in. in diameter. The model had a 310 stainless steel skin with a nominal thickness of 0.040 in. Iron-constantan thermocouples fusion-welded to the inner surface of the skin provided the information necessary to determine the heat-transfer rates. The pressure model used in Tunnel C had the same external dimensions as the heat-transfer model. One difference exists in the geometry of the two clean configuration heat-transfer models. The radius of the spherical cap of the conical section which had been 15.4 in. (full scale) at the time of the JPL test program was reduced to 9.1 in. (full scale) for the AEDC tests. Figure 1 reflects this difference.

A sketch of the 0.09 scale model used in Tunnel C to obtain heat-transfer rates near the cavities and protuberances representative of the Apollo spacecraft is shown in figure 2. The full-scale shear pads, which are cylinders of dense ablator material designed to transmit shear loads between the spacecraft and the service module during the launch phase of the mission, are

6.5 in. in diameter and protrude 0.55 in. above the surface. The full-scale scimitar antenna housing is 2.1 in. wide, extending 8.1 in. above the surface at its peak. The full-scale umbilical fairing protrudes 3.1 in. above the surface. The windward tower well is a cavity roughly 14.8 in. long by 5.5 in. wide with a maximum depth of 4.6 in. full scale. These full-scale dimensions should be multiplied by 0.09 to obtain the actual model "dimensions" for the surface irregularities.

The model shell was constructed of 310 stainless steel with a nominal skin thickness of 0.040 in. Protuberances were secured to the model with screws and were constructed of either a ceramoplastic or 310 stainless steel. The model was instrumented with 30-gage iron-constantan thermocouples, fusion-welded to the inside surface of the model. The support sting was 2.00 in. in diameter and made an angle of 30° with the axis of symmetry.

RESULTS AND DISCUSSION

The experimental investigation of the heat transfer to the Apollo reentry configuration has made use of several different facilities. As noted in reference 1, the pressure and heat-transfer-rate distributions for the clean configuration are essentially independent of flow conditions and of the test facility for hypersonic, laminar flow. Therefore, since the primary purpose of the clean configuration data in the present report is to show the effect of angle-of-attack changes, not all of the data obtained are presented. Most of the data presented herein were obtained in Tunnel C at AEDC. These data are supplemented in some instances by measurements from the 21-in. HWT at JPL. In addition, heat-transfer measurements from Tunnel C are provided to illustrate the influence of cavities and protuberances. A summary of the test conditions covered in this report is given in table I.

Clean Configuration, Pressure Distribution

The pressure distribution in the pitch plane of the reentry configuration is presented in figure 3 for several angles of attack from 0° to 33°. The experimental pressures, measured in Tunnel C at a Reynolds number of 1.1×10^6, have been divided by the calculated value of the stagnation pressure behind a normal shock. Since the maximum pressure measured on the model was greater than the calculated stagnation pressure, the experimental pressure ratios p_l/p_t are seen to exceed unity slightly. The maximum difference is less than 2 percent.

The experimental pressure distribution is compared with the modified Newtonian pressure distribution which is calculated using the expression:

$$\frac{p_l}{p_t} = \cos^2\theta + \frac{p_\infty}{p_t}\sin^2\theta$$

The experimental pressures differ significantly from the modified Newtonian pressures only near the edge of the spherical heat shield, and, for the nonzero angle-of-attack cases, near the stagnation point.

For reference, an S/R of 0.965 defines the tangency point of the spherical heat shield and the toroidal surface. An S/R of 1.08 locates the maximum body radius.

Since the location of the stagnation point is a factor in the calculation of a valid heating-rate distribution, accurate definition of the stagnation point is needed. Figure 4 presents a comparison of the position of the stagnation point as a function of angle of attack as determined by oil-flow studies (ref. 3), pressure measurements of reference 3, pressure measurements from Tunnel C, and modified Newtonian theory. Modified Newtonian theory represents the limiting case of flow at a very high free-stream Mach number. For the Tunnel C tests the location of the maximum measured pressure was assumed to be the stagnation point. Because of the limited number of pressure orifices on the model and the accuracy of the pressure measurements, there are significant variations in the experimental stagnation point. However, the stagnation point locations determined using the Tunnel C pressure data agree with the locations determined from the pressure data of reference 3. Only for zero angle of attack does the experimentally determined stagnation point coincide with the Newtonian location. For the nonzero angle-of-attack cases, the experimental location is nearer the axis of symmetry than is the Newtonian stagnation point. For the purposes of this report, the stagnation point is assumed to be defined by the experimental pressure distribution.

The pressures measured at four locations in the pitch plane are presented as a function of the angle of attack in figure 5. The experimental pressures are compared with the modified Newtonian values. The pressures calculated using modified Newtonian theory are within 10 percent of the pressures measured at the orifice located at an S/R of 0.80 in the $\lambda = 180°$ plane. At the axis of symmetry (fig. 5(b)), the modified Newtonian pressures are within 3 percent of the experimental values. Figure 5(c) presents data at an S/R of 0.8 in the $\lambda = 0°$ plane, where theoretical pressures are within ± 10 percent of the measured values. Modified Newtonian theory indicates that this orifice should correspond to the stagnation point when $\alpha = 19°$. However,

experimental data indicate that this orifice becomes the stagnation point when the angle of attack is between 25° and 35°. Figure 5(d) presents pressure data at an S/R of 1.03 in the $\lambda = 0°$ plane, which is on the toroidal section of the command module (CM). Although the change in pressure for a given angle-of-attack change is approximately the same for both measured and theoretical pressures, modified Newtonian pressures are as much as 50 percent higher than the experimental values. It is apparent from figures 3 to 5 that, in general, modified Newtonian theory agrees with the measurements qualitatively, but not always quantitatively.

The experimental pressure distribution along the windward-most conical generator (the $\lambda = 0°$ plane) is presented in figure 6 for several angles of attack from 0° to 33°. The extent of the conical generator is indicated in this figure. For zero angle of attack the pressure along this ray is essentially constant, being approximately $0.012\ p_t$. For $\alpha = 10°$, the pressure measured at several orifices is actually lower than for the zero angle-of-attack case. The local pressure increases slightly as the angle of attack is increased to $\lambda = 15°$, but remains essentially constant. Thus, the pressure distribution is essentially constant along the conical generator for angles of attack of 0°, 10°, and 15°, indicating a region of separated flow. At an angle of attack of 20° the pressure distribution remains essentially constant, but the pressure is 50 percent above the pressure measured at the same orifice at 15°. The measurements at angles of attack of 25° and 33° show that the pressure distribution on the windward ray varies inversely with distance along the surface, indicating the flow is attached. For comparison, the free-stream static pressure is approximately $0.0075\ p_t$ for the test conditions, which are a free-stream Reynolds number of 1.1×10^6 at a free-stream Mach number of 10.18.

Figure 7 presents constant pressure contours over the entire CM for angles of attack of 20°, 25°, and 33°. The forebody data are presented as an azimuthal equidistant projection, whose origin is the geometric center of the spherical heat shield. The apex of the conical portion of the CM was the center for the development of the afterbody pressure contours. The location of the pressure orifices are indicated by the crosses on the figure. Also shown is the position and extent of the sting for the $\lambda = 180°$ plane.

Flow over most of the forebody is subsonic; that is, the local pressure ratio exceeds $0.53\ p_t$ for angles of attack of 20° and 25°. The area of the forebody where flow is subsonic is considerably less for an angle of attack of 33°. Over the windward afterbody for $\alpha = 33°$, the local pressure varies inversely with S/R for a given conical generator, or with λ for a fixed S/R coordinate. As mentioned previously, the flow in this region is attached. In all three cases there exists a region of increased pressure upstream of the sting

(the contours centered about the 135° ray). The increase may be attributed to the presence of the sting, which had a circular cross section. For an angle of attack of 20°, the pressure at the four orifices immediately upstream of the sting in the $\lambda = 180°$ plane is approximately constant, being between 0.0100 and 0.0115 p_t. Similar comments hold for the other two angles of attack. Hence, the exact extent and severity of pressure perturbations due to the presence of the sting is not defined.

Clean Configuration, Heat-Transfer-Rate Distribution

The experimental pressure data presented above have been used to calculate the heat-transfer-rate distributions. The equation of Lees (ref. 7) is used to obtain the heating rate as a function of position:

$$\dot{q} = 0.50\left(N_{Pr}\right)^{-0.67}\left(\rho_t\mu_t\right)^{0.5}h_t F(s)$$

where

$$F(s) = \frac{\dfrac{p_l}{p_t}\left(\dfrac{\mu_l}{\mu_t}\dfrac{T_t}{T_l}\right)V_l r_o^{\,k}}{\left[2\displaystyle\int_o^x \frac{p_l}{p_t}\left(\frac{\mu_l}{\mu_t}\frac{T_t}{T_l}\right)V_l r_o^{2k}\,dx\right]^{\frac{1}{2}}} \tag{1}$$

If equation (1) is divided by a suitable reference heating rate, the resulting dimensionless expression provides a valid heat-transfer distribution. The stagnation-point heat-transfer rate for the reentry configuration at zero angle of attack is chosen as the reference value. It is given by (ref. 7):

$$\dot{q}_{t)\alpha=0°} = 0.50\left(N_{Pr}\right)^{-0.67}\left(\rho_t\mu_t\right)^{0.5}h_t\sqrt{2}\sqrt{\left(\frac{dV_l}{dS}\right)_{t)\alpha=0°}} \tag{2}$$

Since flow over the zero angle-of-attack reentry configuration is axisymmetric and the stagnation-point velocity gradient is very nearly Newtonian, $\dot{q}_{t)\alpha=0^\circ}$ may be reliably evaluated by accounting for a small correction. The experimental velocity gradients reported in references 8 and 9 are approximately 12 percent greater than Newtonian.

The heating-rate distribution for the pitch plane of the forebody is presented in figure 8. The calculated distributions were obtained from the relation (which is the ratio of equation (1) to equation (2)):

$$\frac{\dot{q}}{\dot{q}_{t)\alpha=0^\circ}} = \frac{1}{2\sqrt{\left(\frac{dV_1}{dS}\right)_{t)\alpha=0^\circ}}} \left\{ \frac{\frac{p_1}{p_t}\left(\frac{\mu_1}{\mu_t}\frac{T_t}{T_1}\right) V_1 r_o^{\,k}}{\left[\int_o^x \frac{p_1}{p_t}\left(\frac{\mu_1}{\mu_t}\frac{T_t}{T_1}\right) V_1 r_o^{2k}\, dx\right]^{\frac{1}{2}}} \right\}_\alpha \qquad (3)$$

The distance x is measured along the body surface from the experimentally determined stagnation point. The local air properties are determined using the perfect gas relation of reference 10 in conjunction with the pressure distributions measured in Tunnel C at a free-stream Reynolds number of 1.1×10^6. Since equation (3) is indeterminate at the stagnation point, the distribution in this region represents a fairing of the results obtained on either side of the stagnation point.

The heating rates measured in Tunnel C at a nominal free-stream Mach number of 10 for free-stream Reynolds numbers from 0.2×10^6 to 1.2×10^6 are presented in figures 8(a), 8(c), and 8(d) for angles of attack of 0°, 28°, and 33°, respectively. These data are considered representative of the hypersonic, laminar heat-transfer data. Since no data are available at these test conditions for $\alpha = 20^\circ$, measurements obtained in the 21-in. HWT at JPL are presented as typical (fig. 8(b)). The flow conditions for the JPL tests included free-stream Mach numbers from 6 to 9 with free-stream Reynolds numbers from 0.17×10^6 to 0.62×10^6.

Since the reentry configuration at zero angle of attack is axisymmetric, a value of $k = 1$ was used in equation (3) for this case. The experimental heating rates are within ± 10 percent of the calculated values, except on the toroid, where Lees' equation overestimates the measured values by as much as 20 percent. Appreciable scatter of the measured heat-transfer rates occurs over the spherical heat shield.

For angles of attack other than zero, flow in the pitch plane of the reentry configuration is neither two-dimensional nor axisymmetric. Heat-transfer rates measured in the pitch plane would be expected to fall between the level of heating for two-dimensional flow and the level for axisymmetric flow. Figures 8(b) to 8(d) compare the experimental heating rates for nonzero angle of attack with the distributions calculated for two-dimensional flow and for axisymmetric flow (using $k = 0$ and $k = 1$, respectively, in eq. (3)). For either value of k, the stagnation-point heating rate for the zero angle-of-attack configuration remains the denominator of the dimensionless heat-transfer rate. Because $\dot{q}_{t)\alpha=0^\circ}$ is used as a reference in both calculations, the difference between the theoretical distributions in figures 8(b) to 8(d) represents the difference between the local heat transfer for two-dimensional flow and that for axisymmetric flow at a given angle of attack.

Although there is significant scatter in the measured heating rates at $\alpha = 20^\circ$, the measurements fall approximately midway between the calculated values. For angles of attack of 28° and 33°, the experimental heat-transfer-rate ratios obtained in Tunnel C exhibit little scatter. Except near the toroidal regions, the measured heating rates are about midway between the two calculated levels. Near the windward corner the heat-transfer rate calculated for two-dimensional flow is close to the measured value.

The heat-transfer rate at three thermocouples in the pitch plane of the spherical heat shield are presented in figure 9, as a function of angle of attack. At zero angle of attack the heating rates calculated assuming axisymmetric flow agree with the measured values. As the angle of attack is increased, heat-transfer rates at the axis of symmetry (fig. 9(a)) are approximately midway between the two calculated levels. The heat transfer at the windward-most thermocouple (fig. 9(b)) approaches the level for two-dimensional flow, while for the most leeward thermocouple (fig. 9(c)) the heat-transfer rate remains close to the level predicted for axisymmetric flow. From figures 8 and 9 it is apparent that, except for zero angle of attack, no single value for k can be used to calculate heat-transfer rates which agree with measurements in the forebody pitch plane.

The experimental heat-transfer-rate distribution along the windward-most conical generator is compared with theoretical distributions in figure 10. Two approaches were used to obtain theoretical heating rates. One used the equation for attached, laminar flow over a flat plate:

$$\dot{q} = 0.332 \left(Re_x^*\right)^{0.5} \left(N_{Pr}^*\right)^{0.333} \frac{k^*}{x} \left(T_{aw} - T_w\right) \tag{4}$$

The local properties were evaluated using the experimental pressure distribution and Eckert's reference temperature (ref. 11). The second method used Lees' equations. Since the flow over the forebody is axisymmetric for the low-angle-of-attack case, k is chosen to be one to compute the forebody integral in the denominator of equation (3). At the maximum body radius the value of the integral is divided by R^2, thereby adjusting it to the value for two-dimensional flow. Calculations proceed over the afterbody, assuming k to be 0, or two dimensional. The form of the equation used for the zero angle of attack afterbody heating is:

$$\frac{\dot{q}}{\dot{q}_{t)\alpha=0^\circ}} = \frac{1}{2\sqrt{\left(\frac{dV_1}{dS}\right)_{t)\alpha=0^\circ}}} \left(\frac{\frac{p_1}{p_t}\left(\frac{\mu_1}{\mu_t}\frac{T_t}{T_1}\right)V_1}{\left[\frac{1}{R^2}\int_0^{S_c}\frac{p_1}{p_t}\left(\frac{\mu_1}{\mu_t}\frac{T_t}{T_1}\right)V_1 r_o^{2k}\,dx + \int_{S_c}^{x}\frac{p_1}{p_t}\left(\frac{\mu_1}{\mu_t}\frac{T_t}{T_1}\right)V_1\,dx\right]^{\frac{1}{2}}} \right)_{\alpha=0^\circ} \tag{5}$$

For zero angle of attack the measured heat-transfer rates are roughly one-half the theoretical values over the conical portion of the afterbody. For angles of attack of 20°, 28°, and 33°, the flow was assumed planar for the entire calculation using Lees' equations. (Near the windward corner, the measured heat-transfer rates were in approximate agreement with the two-dimensional calculations, as shown in figure 8.) The theoretical distribution is essentially the same for either method and agrees approximately with the experimental distribution.

The hypersonic, laminar heat-transfer-rate distribution for the entire clean configuration is given in figure 11. The constant heating-rate contours represent an interpretive fairing of the measurements. For an angle of attack of 20°, the data were obtained at free-stream Mach numbers from 6 to 9 with Reynolds numbers from 0.17×10^6 to 0.62×10^6. The measurements at angles of attack of 25° and 33° were obtained at a Mach number of 10 for free-stream Reynolds numbers from 0.2×10^6 to 1.2×10^6. The forebody data are presented as an azimuthal equidistant projection, whose origin is the geometric center of the spherical heat shield. The apex of the conical portion of the CM was chosen as the center for the afterbody data. The thermocouple locations for these tests are given by the crosses on the figure. The location and extent of the sting in the $\lambda = 180^\circ$ plane is indicated. The cross section of the sting was circular.

Cavities and Protuberance Model

The locations of the cavities and the protuberances are illustrated by the azimuthal equidistant projections of figure 12 and by the sketch of figure 3. The dimensions of the cavities and protuberances are provided in the section on facilities and models. The thermocouple locations on the 0.09 scale stainless steel model used in Tunnel C are designated by crosses. Since some of the thermocouples were shaken loose during the test program, interference heating data were not obtained at all thermocouples for every test condition. Except for the region just upstream of shear pad no. 3, the thermocouple failures were scattered around the model. Sixteen of the thermocouples are specified by number. Detailed interference heating data at these locations are presented.

The influence of the shear pads and the umbilical fairing on the heat transfer to the spherical heat shield is indicated in figure 13. The data are presented as interference heating factors; that is, the ratio of the heat-transfer rate measured in the presence of the protuberances to the heat-transfer rate measured at the same thermocouple on the clean CM. At thermocouples external to the interference-heating-factor contours designated $q_{ihf} = 1$, the heat transfer was unaffected by the presence of the protuberances. Thus, the presence of the shear pads and the umbilical fairing did not affect the heat-transfer rates in the pitch plane. Since the pitch-plane heating rates were found to agree with laminar heating rates measured on a clean configuration, it was concluded that the unperturbed flow was laminar for both Reynolds numbers.

A region of increased heating downstream of shear pad no. 1 is indicated in figure 13. The region of increased heating is located approximately by a line from the stagnation point (which is indicated by the diamond of fig. 13) through the shear pad. Increasing the angle of attack not only altered the region affected by the presence of the shear pad, as expected, but also increased the size of the affected area. Although interference heating factors were as high as 2.7, the majority of the affected area experienced an increase of less than 50 percent. These interference heating factors agree approximately with those reported in reference 6. Shear pad no. 1, which was in a subsonic flow regime, did not affect the heat transfer upstream of the pad.

Interference-heating-factor contours in the vicinity of shear pad no. 3 and the umbilical fairing are also shown. Since, as noted previously, several thermocouples just upstream of this shear pad failed, the fairings in this region are interpretive. The presence of shear pad no. 3 more than doubled the heating just upstream, as well as downstream, of the pad. The pad lies in the transonic region for $\alpha = 22°$ and in the supersonic region for $\alpha = 33°$.

Just ahead of the umbilical fairing, downstream of shear pad no. 3, heating rates were as much as eight times the clean configuration measurements. This level of increase agrees with that reported in reference 6.

The interference heating factors at five locations near shear pad no. 1 are presented in figure 14 for angles of attack from 18° to 37°. The measurements at thermocouples 1, 2, and 3 (see fig. 12 for locations) illustrate the effect of the angle of attack noted in figure 13. As the angle of attack increases, the perturbed area shifts toward the $\lambda = 90°$ plane. At thermocouple 1 (which is in the $\lambda = 50°$ plane) the heat-transfer rates are the same as the clean configuration rates for the angle-of-attack range considered. At thermocouple 2 (which is in the $\lambda = 57°$ plane) the heating rates at $\alpha = 18°$ are 50 percent higher than the clean configuration values, but decrease to the unperturbed rates for angles of attack greater than 30°. The heat transfer at thermocouple 3 (in the $\lambda = 68°$ plane) is unaffected by the shear pad when the angle of attack is less than 25°. Measurements at thermocouple 4 are presented in figure 14(d) as representative of interference heating factors immediately behind the shear pad. The heat-transfer rates are significantly higher than the smooth body rates. At thermocouple 5 the interference heating factors increase rapidly with angle of attack, as might be expected.

At thermocouple 5, for a given angle of attack, the increase in heating is much greater at the lower Reynolds number. At thermocouple 4 the opposite is true, as the higher interference heating factors are observed at the higher Reynolds number. The interference heating factors at thermocouples 1, 2, and 3 apparently do not depend on the free-stream Reynolds number. Thus, a general statement regarding the effect of the free-stream Reynolds number is not possible.

Figure 15 provides interference heating factors at four thermocouples in the vicinity of shear pad no. 3 for angles of attack from 18° to 37° at both test Reynolds numbers. At thermocouple 6, which is just upstream of the shear pad, the heating is significantly increased over the level for the clean configuration. The interference heating factor is directly proportional to the angle of attack, hence the local Mach number. (The local pressure was shown to vary inversely with angle of attack in figure 5(a), so the local Mach varies directly with the angle of attack.) Calculations show that the height of shear pad no. 3 is roughly twice the boundary-layer momentum thickness. Therefore, the increased heating upstream of shear pad no. 3 appears to indicate the presence of a shock-boundary layer interaction. As noted previously, shear pad no. 1 did not affect the heating at thermocouples upstream of it. Since shear pad no. 1 is in a region of subsonic flow, no shock is possible and thermocouples upstream of the pad would not experience the increased heating experienced by thermocouples of shear pad no. 3.

Figure 15(b) provides interference heating factors downstream of the shear pad at thermocouple 7. The heating rates are 2 to 3 times the clean body values and show little dependence on the Reynolds number. Heat-transfer rates at the foot of the umbilical fairing are shown in figures 15(c) and 15(d). The interference heating factors obtained at these two thermocouples are higher at the higher Reynolds number. At thermocouple 8, the interference heating factor varies from 5 to 8, the highest values being observed on the forebody over the entire range of test conditions.

Figure 16 shows interference heating factors observed at thermocouples on the windward side of the afterbody. Due to the limited amount of instrumentation, no attempt was made to fair curves through the data. The presence of scimitar antenna no. 1 (refer to fig. 12 for identification) produced a significant increase in the heat transfer to the thermocouples adjacent to the antenna and to those downstream along the windward-most generator. The maximum increase measured was at the base of the forward edge of the antenna. For these angles of attack the heating at this point was 6 to 7 times the clean-configuration heating for the Reynolds numbers tested. These results correspond to the values reported in reference 6. The heat-transfer rates near tower well no. 1 are increased by as much as a factor of 4.5.

The influence of scimitar antenna no. 1 at thermocouples 10 and 11 is shown in figure 17. At the upstream base of the antenna, thermocouple 10 experienced heating rates as much as 9 times higher than the clean-configuration values. On the windward most conical generator at thermocouple 11, the interference heating factors varied from 1 to 2. At both thermocouples, the interference heating factors are higher at the higher Reynolds number.

The effect of the windward tower well is indicated by figure 18. At thermocouple 12 the heat-transfer rate is influenced only slightly by the presence of the cavity, except at an angle of attack of 22°. For an unknown reason, the interference heating factor at this particular angle of attack is between 2.5 and 3.5 (depending on the Reynolds number). At thermocouple 13 the interference heating factor varied directly with angle of attack. Other thermocouples, both upstream and downstream of the tower well, experienced increases of the order shown here.

Data from the thermocouples on the leeward afterbody are given in figure 19. The measurements at the foot of the air vent are presented in figure 19(a). As might be expected, the interference heating factor varies inversely with α, since the air vent is in the separated region at the higher angles of attack. For angles of attack less than 30°, the interference heating factor is much higher at the higher Reynolds number.

The data from thermocouples 15 and 16 are representative of heat transfer to the leeward afterbody; that is, between the $\lambda = 90°$ and the $\lambda = 270°$ planes. The interference heating factors vary between 0.75 and 1.5, exhibiting no definite dependence on the free-stream Reynolds number on the angle of attack. Since heat-transfer-rates are relatively small over the leeward afterbody, small errors in the measured rates would appear relatively large. The interference heating factors appear to reflect the uncertainty of leeward heat-transfer measurements in the presence of the sting, rather than the influence of the protuberances.

CONCLUDING REMARKS

Heat-transfer-rate and pressure measurements for the clean reentry configuration have been presented over an angle-of-attack range from $0°$ to $33°$. The results, where practical, were compared with theoretical values. For the range of test conditions of the study, the following observations are made:

a. In the pitch plane of the spherical heat shield, the modified Newtonian pressures are in approximate agreement with the measured values, except near the stagnation point and in the vicinity of the toroidal section.

b. In the pitch plane of the spherical heat shield, the experimental heat-transfer-rate distribution lies between the theoretical distribution for axisymmetric flow and the theoretical distribution for planar flow. In both cases the experimental pressure distribution was used to calculate local properties.

c. Either flat plate theory or Lees' equations for planar flow may be used to estimate the heat-transfer-rate distribution along the windward-most generator.

A program was conducted in Tunnel C to investigate the effects of cavities and protuberances on the heat transfer to the Apollo CM. Heat-transfer rates were measured on a clean configuration, and then at the same location with the cavities and protuberances in place. For the range of test conditions, the following comments are made concerning interference effects:

a. The interference heating factors obtained using the stainless steel model agree approximately with those obtained using a phase-change coating on a plastic model.

b. Increased heating was observed in a large area downstream of

shear pad no. 1. Over most of the area, the increase was 50 percent or less, although the heating was almost trebled at some locations.

c. Interference heating factors up to 8 were observed upstream of the umbilical fairing in the wake of shear pad no. 3.

d. The peak heat-transfer rate in the vicinity of antenna housing no. 1 was about 9 times the smooth body value.

e. The heat transfer to the leeward afterbody was apparently unaffected by the cavities and protuberances.

Manned Spacecraft Center
National Aeronautics and Space Administration
Houston, Texas, March 3, 1966

REFERENCES

1. Bertin, John J.: Wind-Tunnel Heating Rates for the Apollo Spacecraft. NASA TM X-1033, 1965.

2. Jones, Jim J.; and Moore, John A.: Shock-Tunnel Heat-Transfer Investigation on the Afterbody of an Apollo-Type Configuration at Angles of Attack Up to 45°. NASA TM X-1042, 1964.

3. Jones, Robert A.: Experimental Investigation of the Overall Pressure Distribution, Flow Field, and Afterbody Heat Transfer Distribution of an Apollo Reentry Configuration at a Mach Number of 8. NASA TM X-813, 1963.

4. Jones, Robert A.: Measured Heat-Transfer and Pressure Distributions on the Apollo Face at a Mach Number of 8 and Estimates for Flight Conditions. NASA TM X-919, 1964.

5. Marvin, Joseph G.; and Kussoy, Marvin: Experimental Investigation of the Flow Field and Heat Transfer over the Apollo-Capsule Afterbody at a Mach Number of 20. NASA TM X-1032, 1965.

6. Jones, Robert A.: Effects of Cavities, Protuberances, and Reaction-Control Jets on Heat Transfer to the Apollo Command Module. NASA TM X-1063, 1965.

7. Lees, Lester: Laminar Heat Transfer over Blunt-Nosed Bodies at Hypersonic Flight Speeds. Jet Propulsion, vol. 26, no. 4, April 1956, pp. 259-269, 274.

8. Stoney, William E., Jr.: Aerodynamic Heating of Blunt-Nose Shapes at Mach Numbers up to 14. NACA RML 58E05a, 1958.

9. Boison, J. C.; and Curtiss, H. A.: An Experimental Investigation of Blunt Body Stagnation Point Velocity Gradient. ARS Journal, February 1959, pp. 130-135.

10. Ames Research Staff: Equations, Tables, and Charts for Compressible Flow. NACA Report 1135 (supersedes NACA TN 1428), 1953.

11. Eckert, E. R. G.: Engineering Relations for Friction and Heat Transfer to Surfaces in High Velocity Flow. d. Aero. Sciences, vol. 22, no. 8, August 1955, pp. 585-587.

TABLE I. - SUMMARY OF TEST CONDITION

Facility	Model	M	Re_D
21-inch HWT, JPL	0.02	6 to 9	0.17×10^6 to 0.62×10^6
Tunnel C, AEDC	0.045	10	0.2×10^6 to 1.4×10^6
Tunnel C, AEDC	[a]0.045	10	1.1×10^6
Tunnel C, AEDC	0.09	10	1.37×10^6 to 2.56×10^6

[a]These test conditions apply to the pressure model.

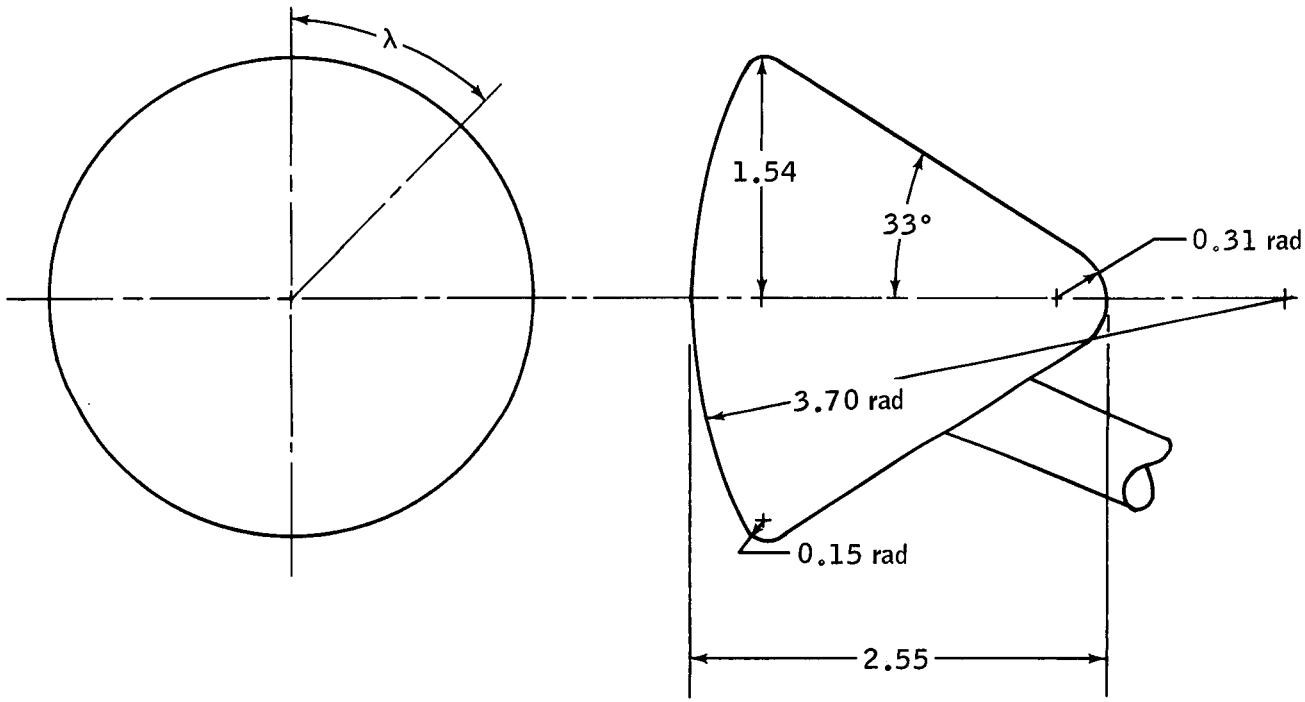

(a) JPL, 0.02 scale model

Figure 1. - Sketch of clean Apollo command module models used in test program. All dimensions in inches.

NASA-S-66-2311 MAR 10

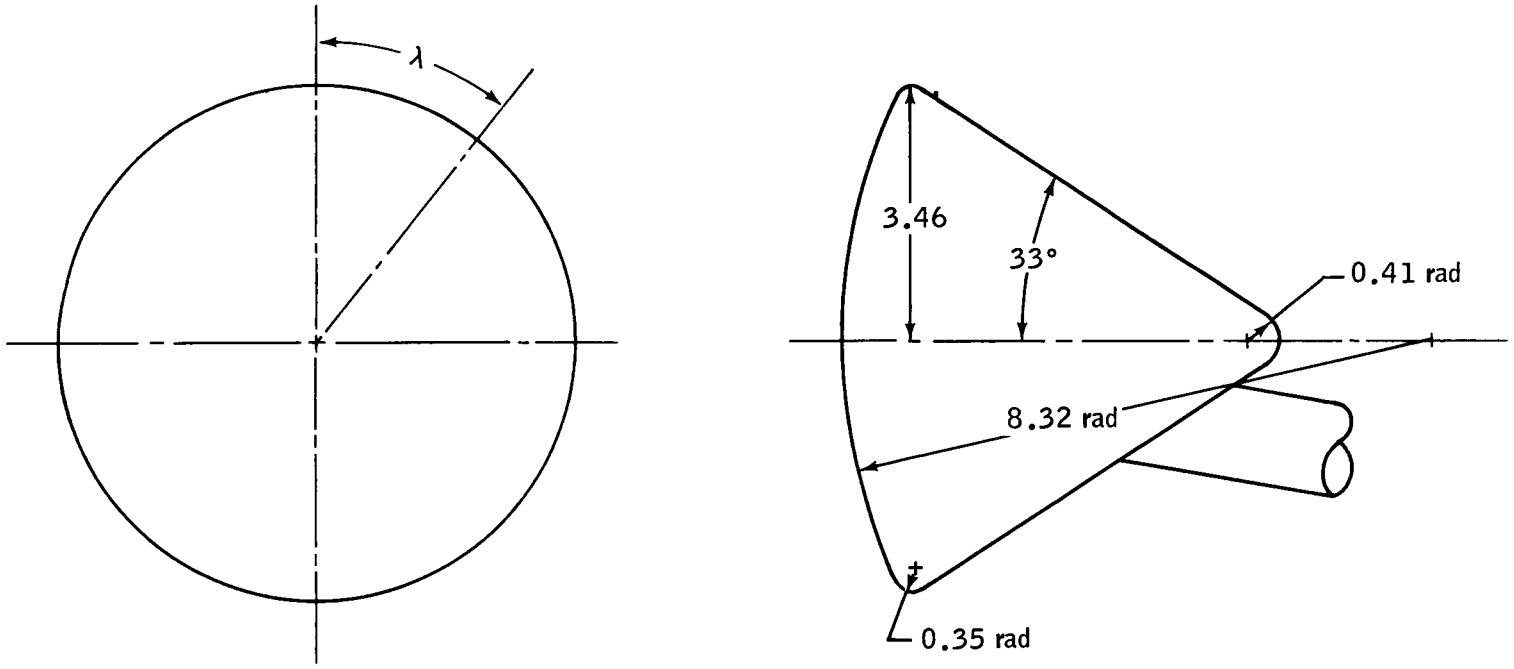

(b) AEDC, 0.045 scale model.

Figure 1. - Concluded.

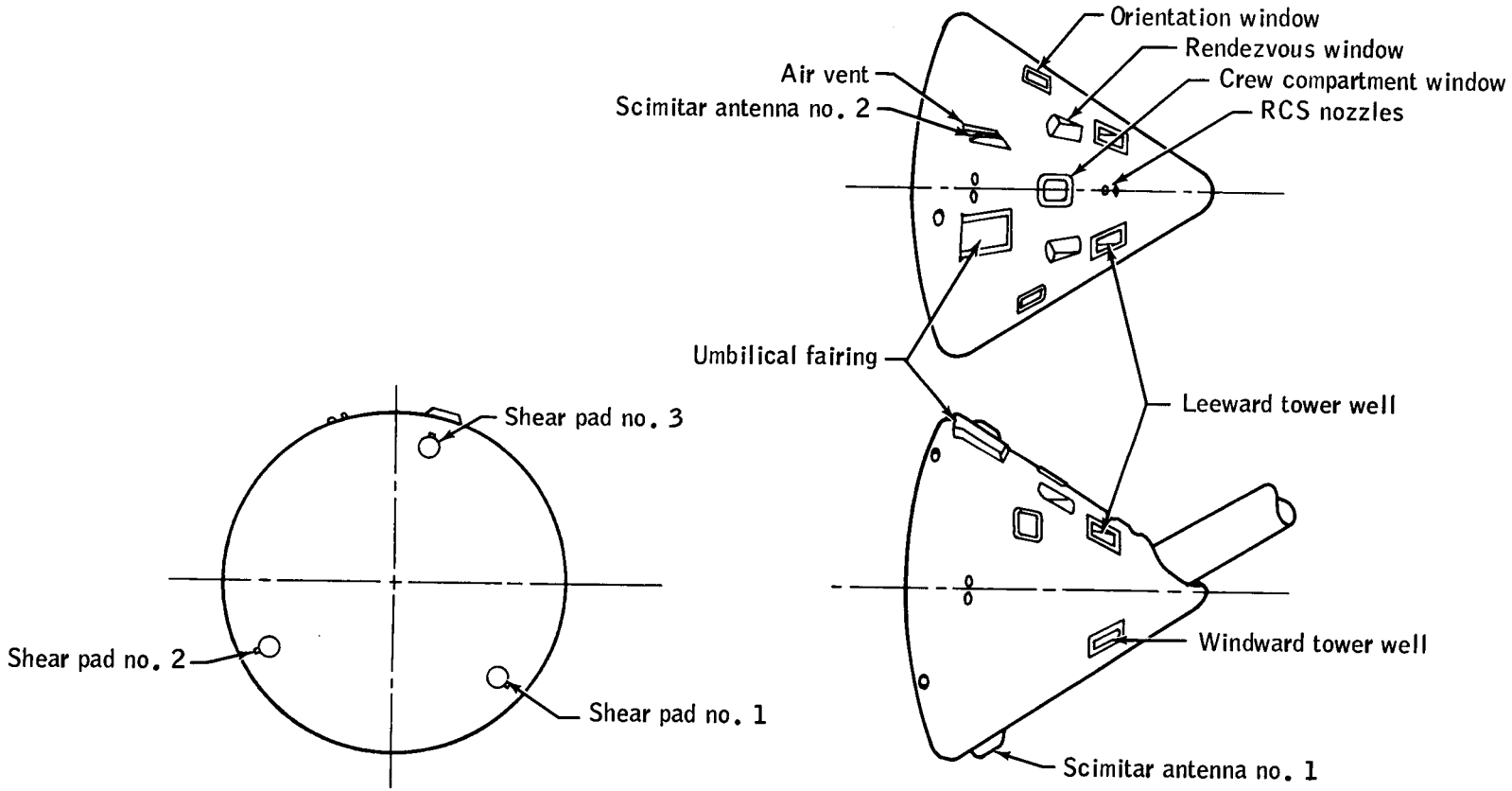

Figure 2. - Sketch of the Apollo command module illustrating the cavities and the proturbances.

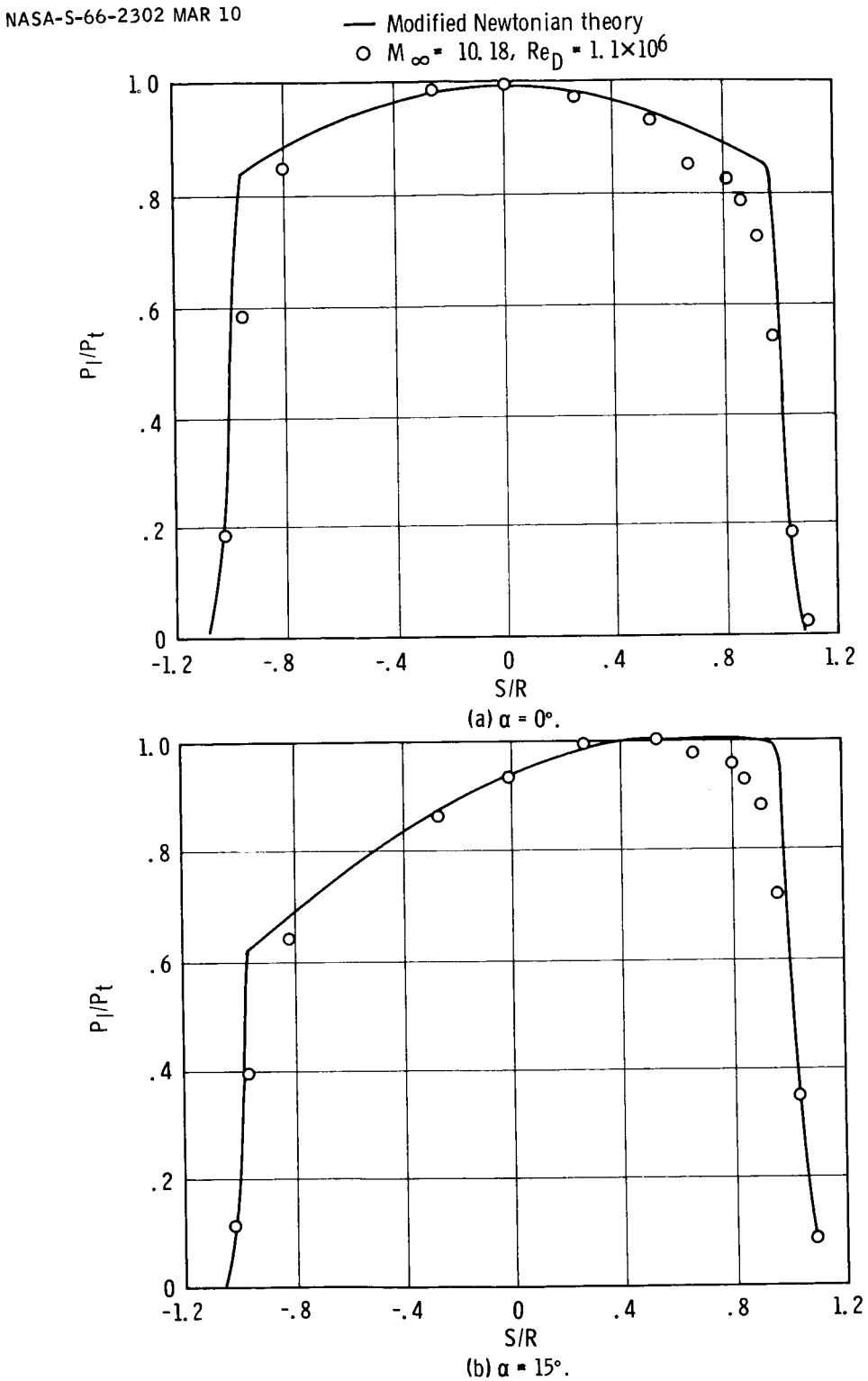

Figure 3. - Pressure distribution for the pitch plane of the spherical heat shield.

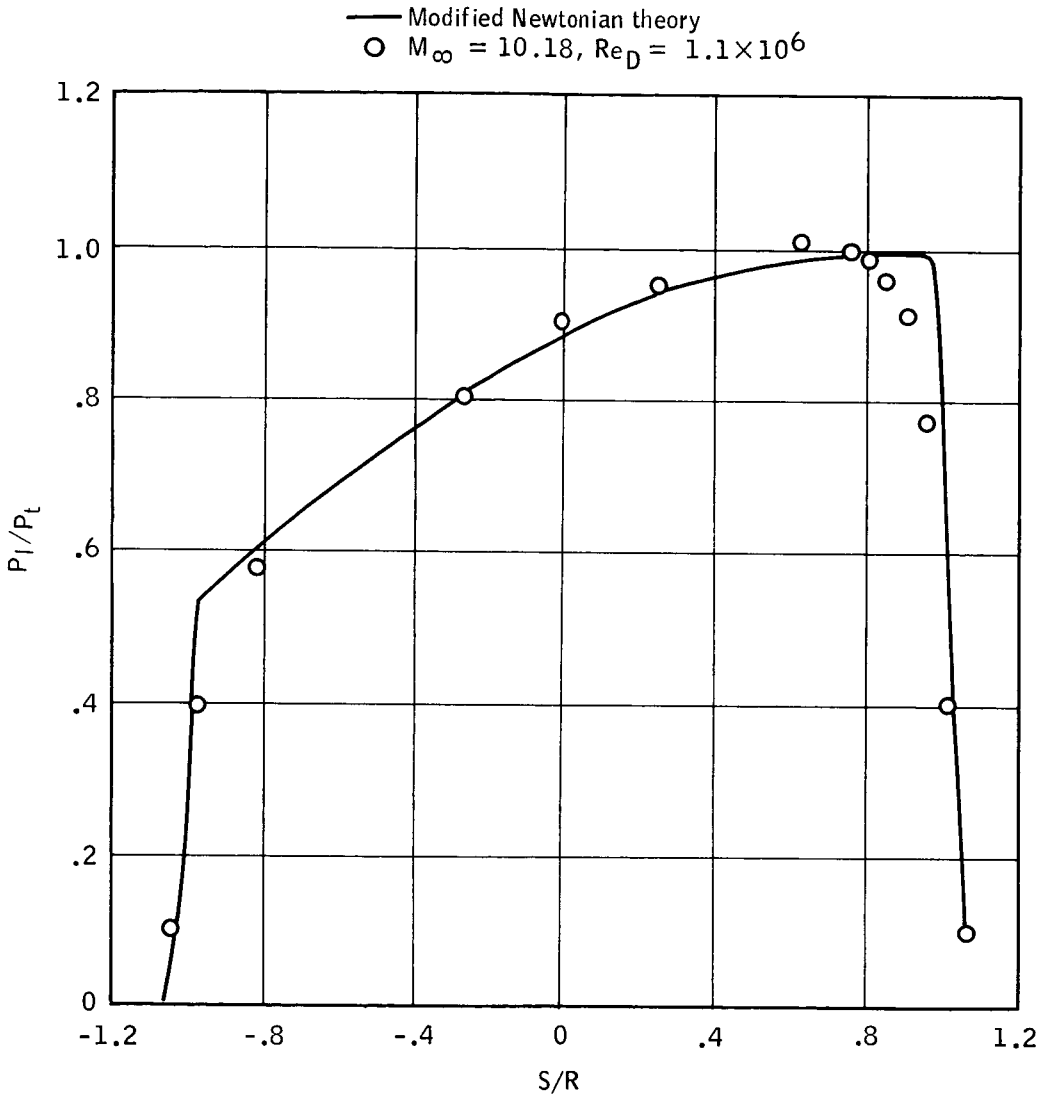

(c) $\alpha = 20°$.

Figure 3. - Continued.

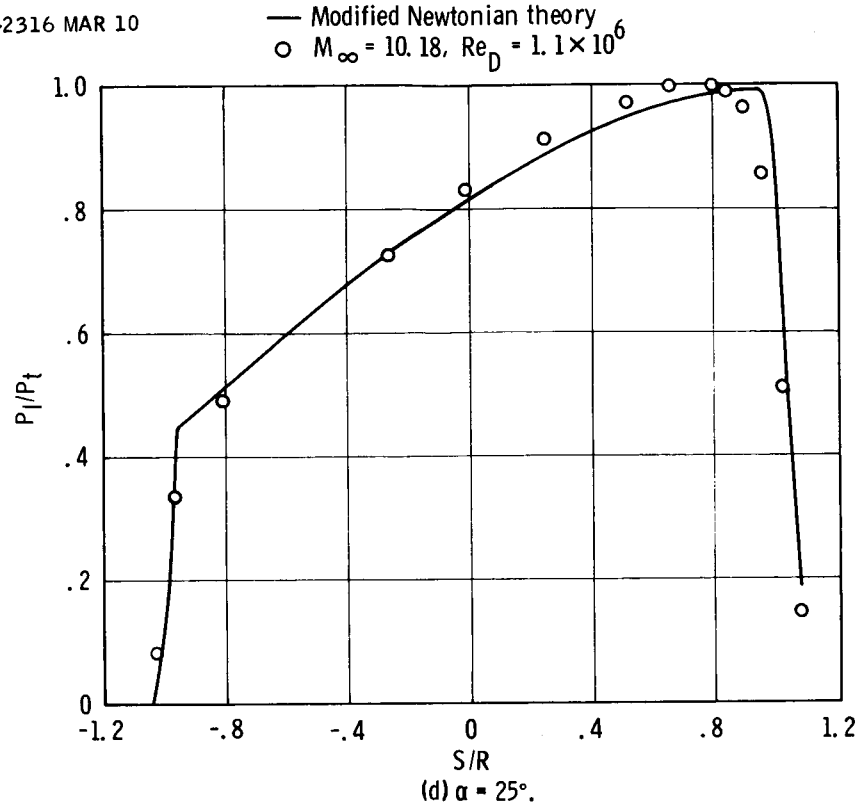

(d) α = 25°.

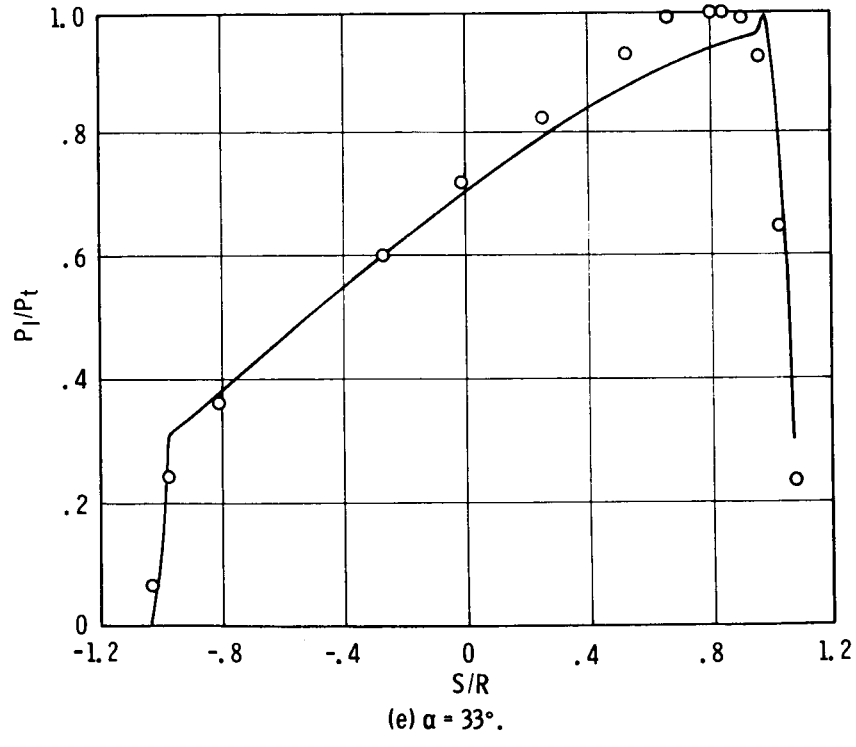

(e) α = 33°.

Figure 3. - Concluded.

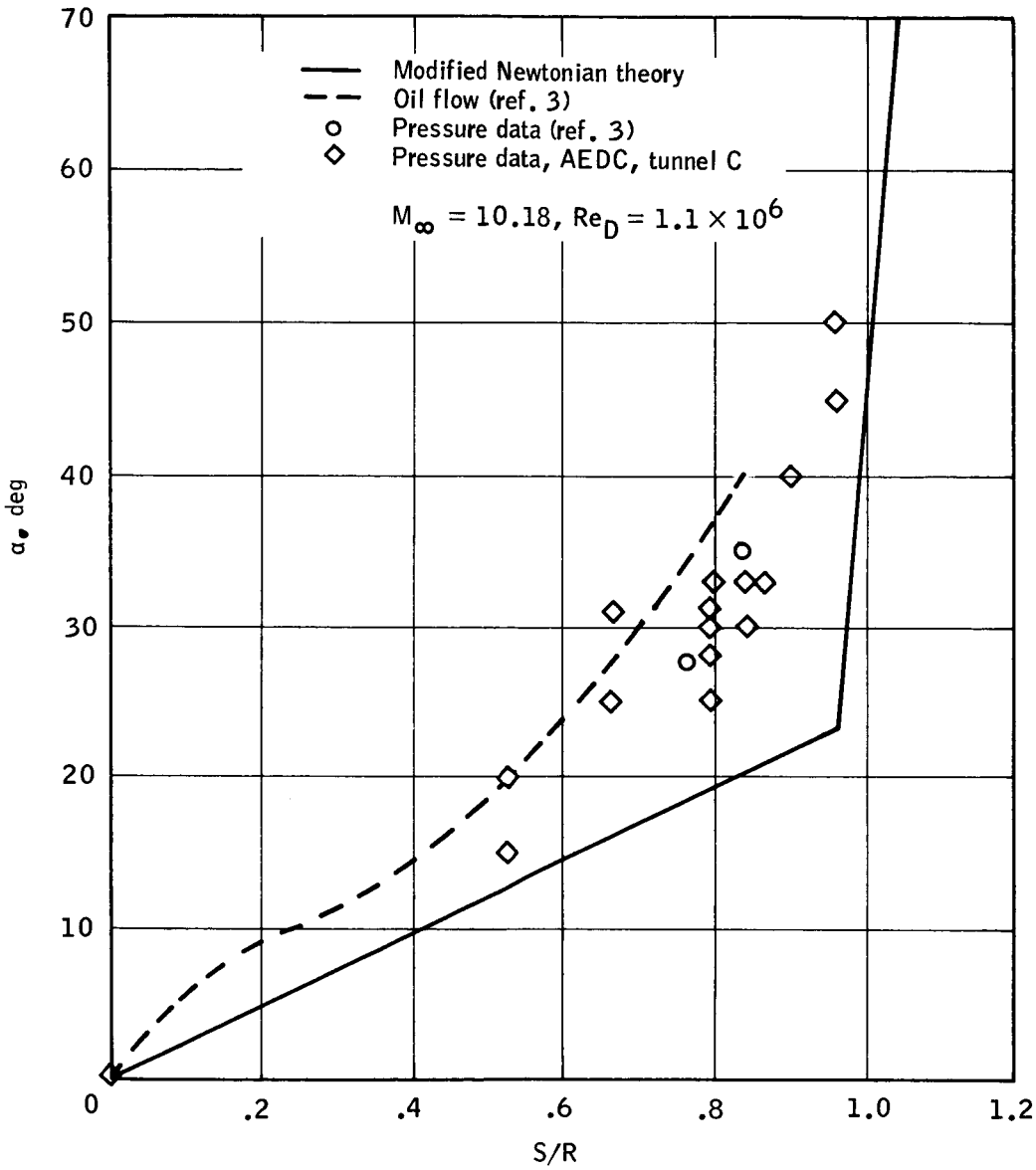

Figure 4. - Location of stagnation point as a function of the angle of attack.

NASA-S-66-2309 MAR 10

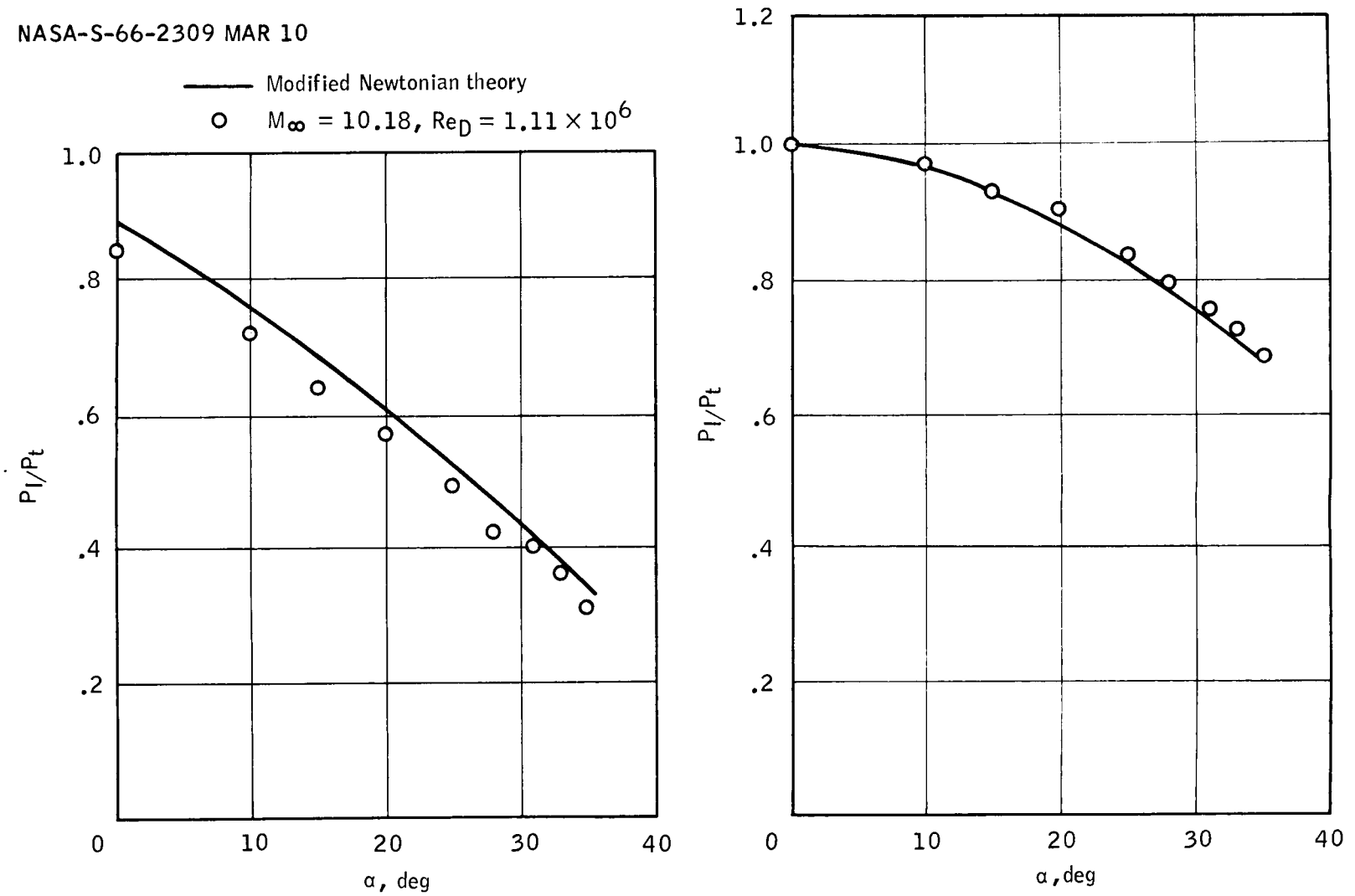

(a) S/R = .8, λ = 180°.

(b) S/R = 0, λ = 0°.

Figure 5. - Forebody pressure as a function of the angle of attack.

NASA-S-66-2300 MAR 10

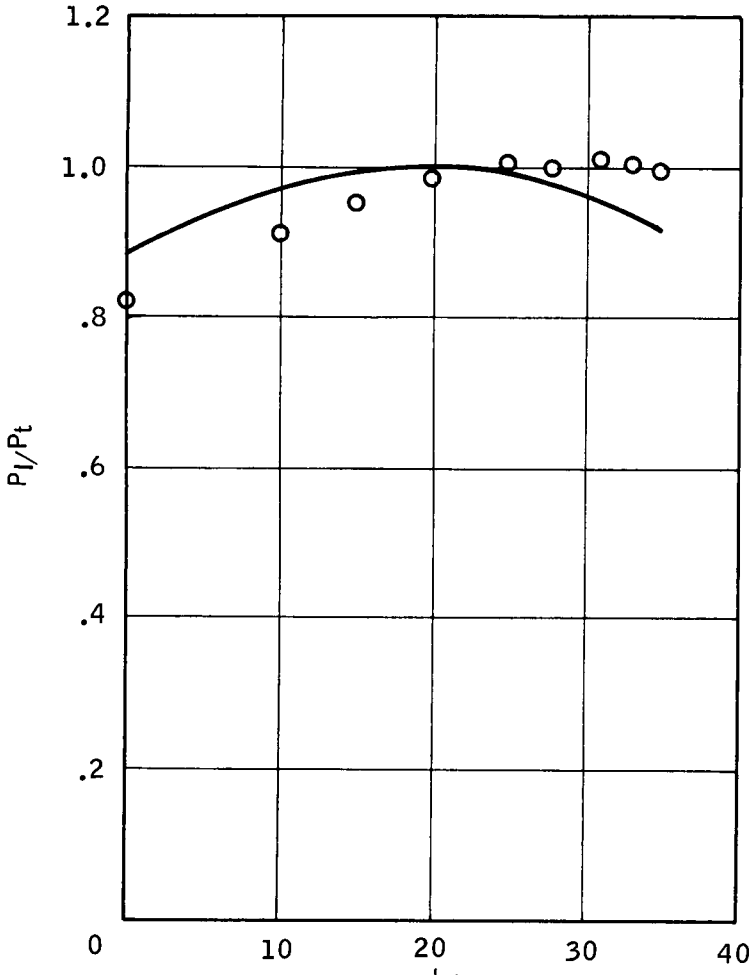

(c) S/R = .8, λ = 0°.

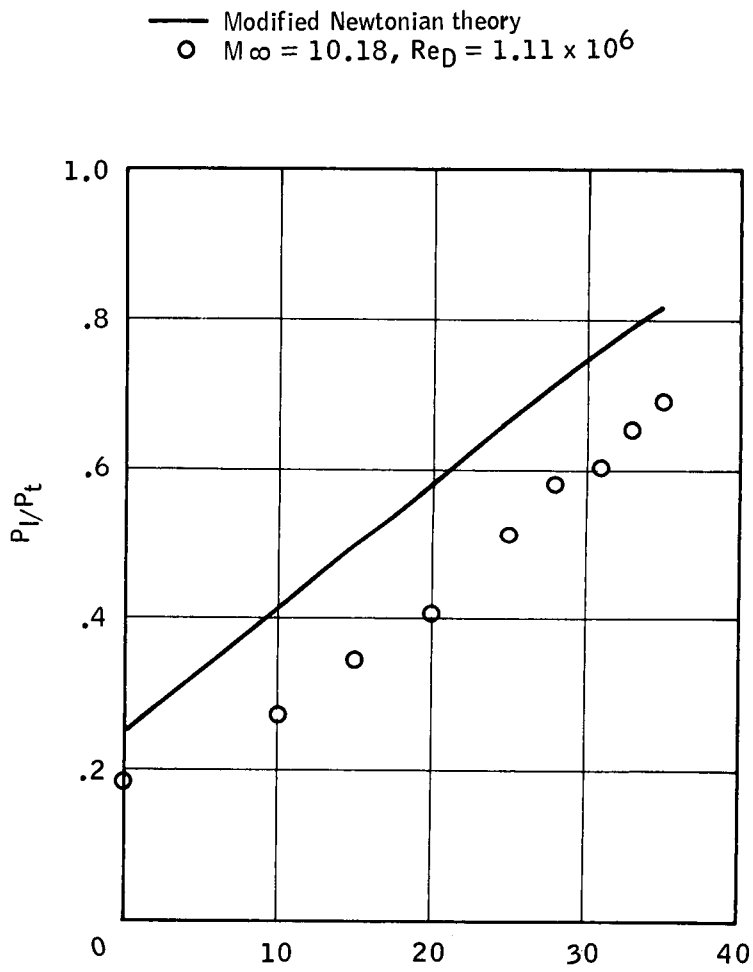

(d) S/R = 1.03, λ = 0°.

Figure 5. - Concluded.

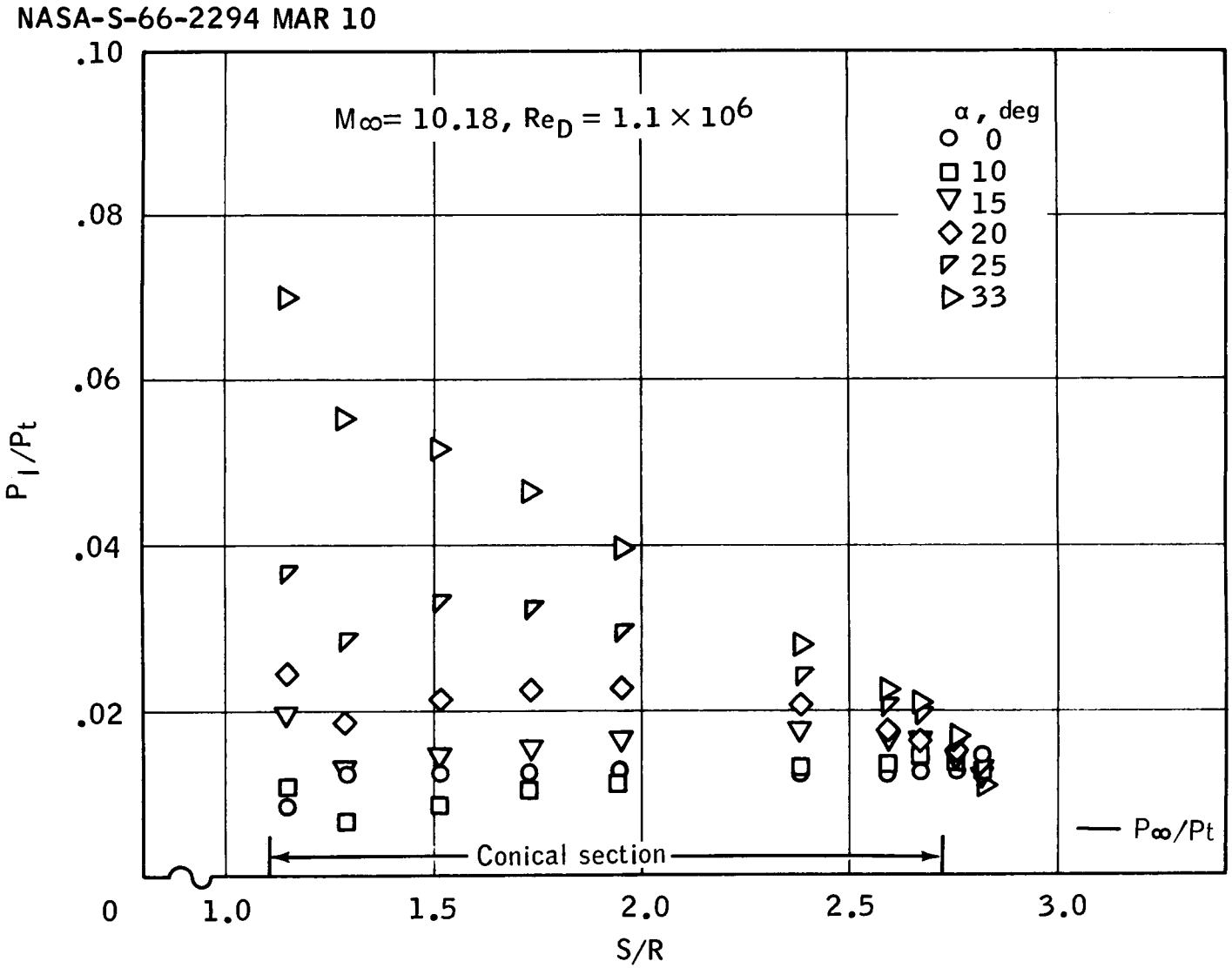

Figure 6. - Pressure distribution along the windward - most conical generator as a function of the angle of attack.

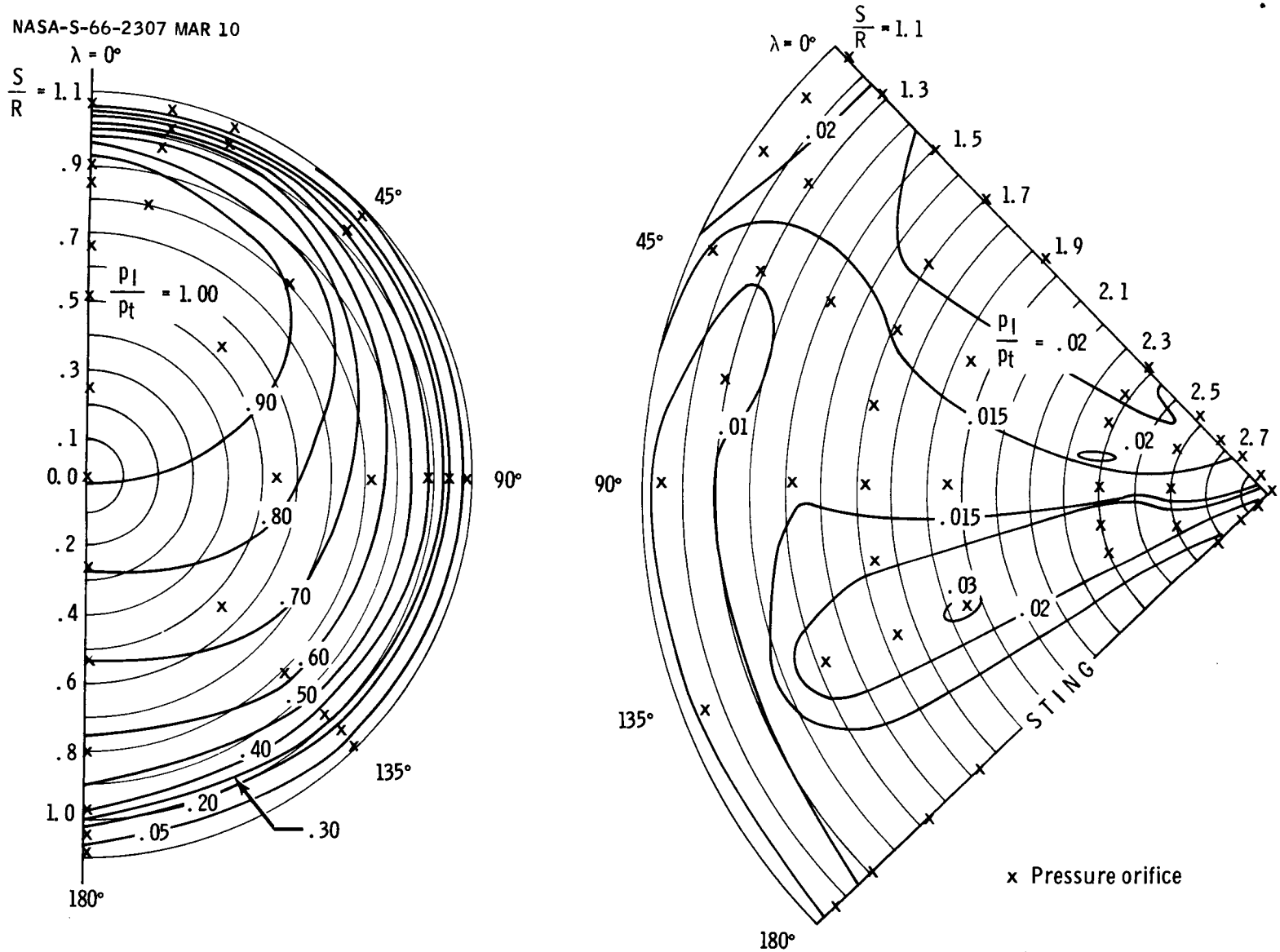

(a) α = 20°

Figure 7. - Overall pressure distribution. $M_\infty = 10.18$, $Re_D = 1.1 \times 10^6$.

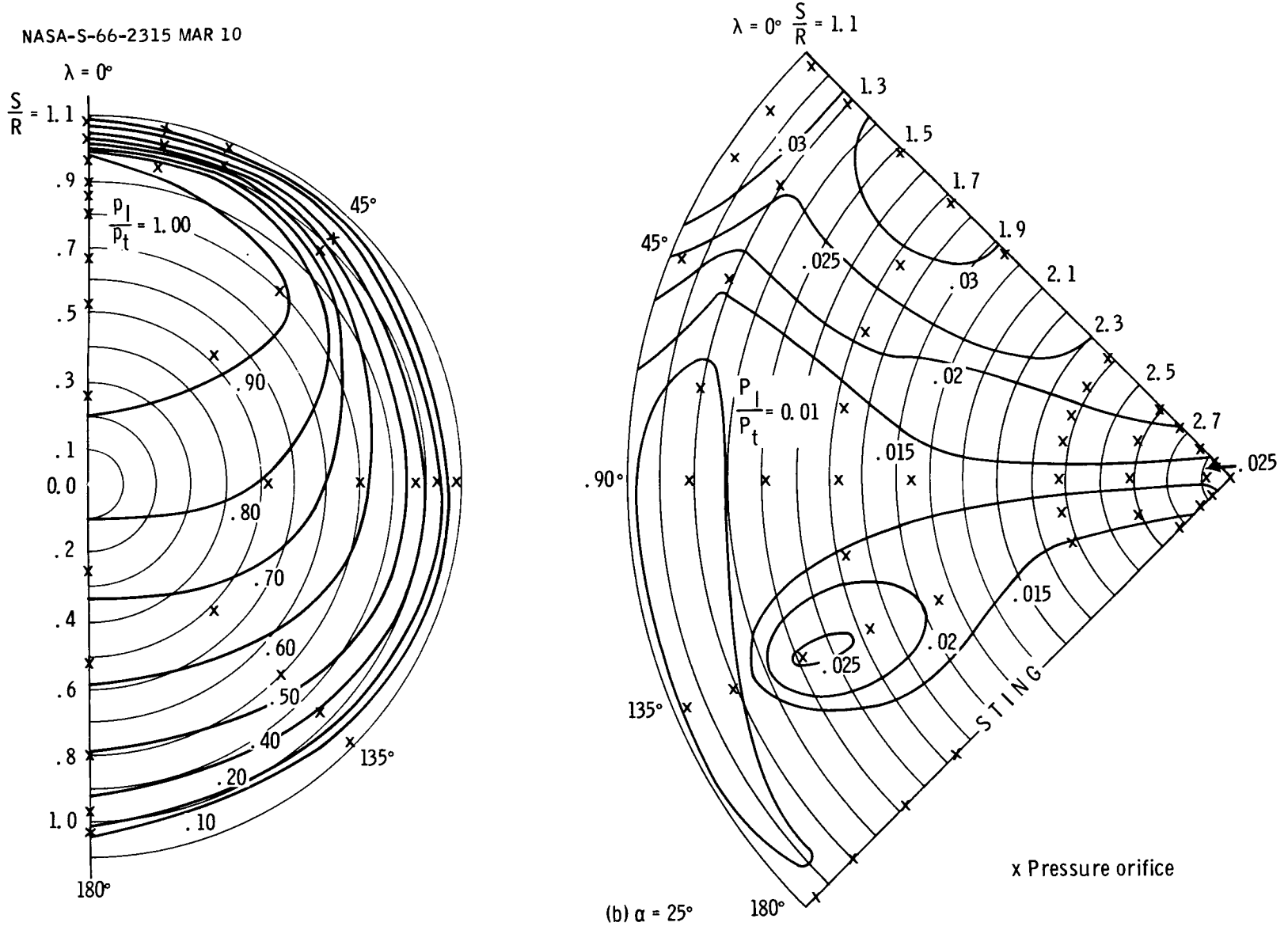

Figure 7. - Continued.

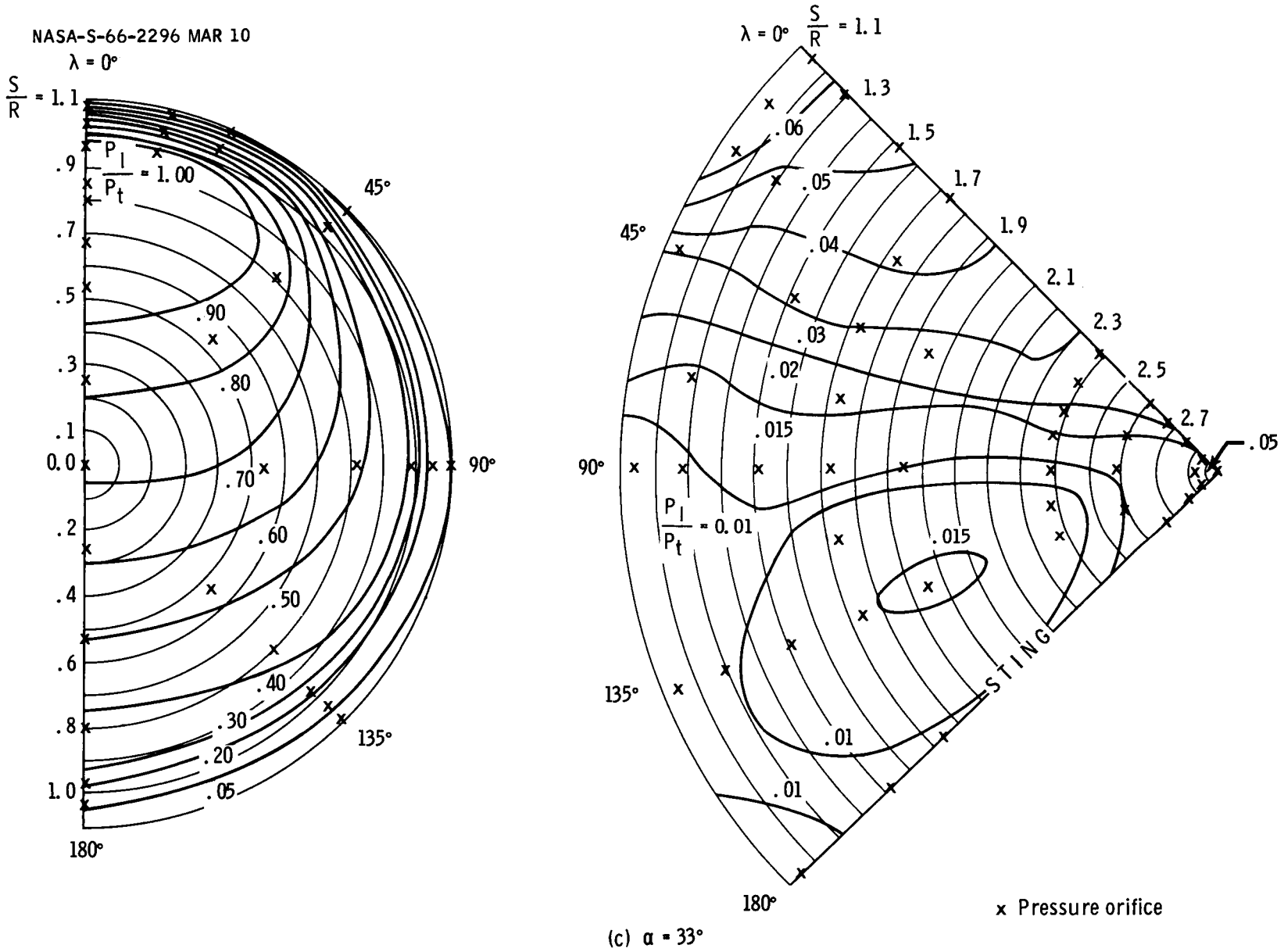

(c) α = 33°

Figure 7. - Concluded.

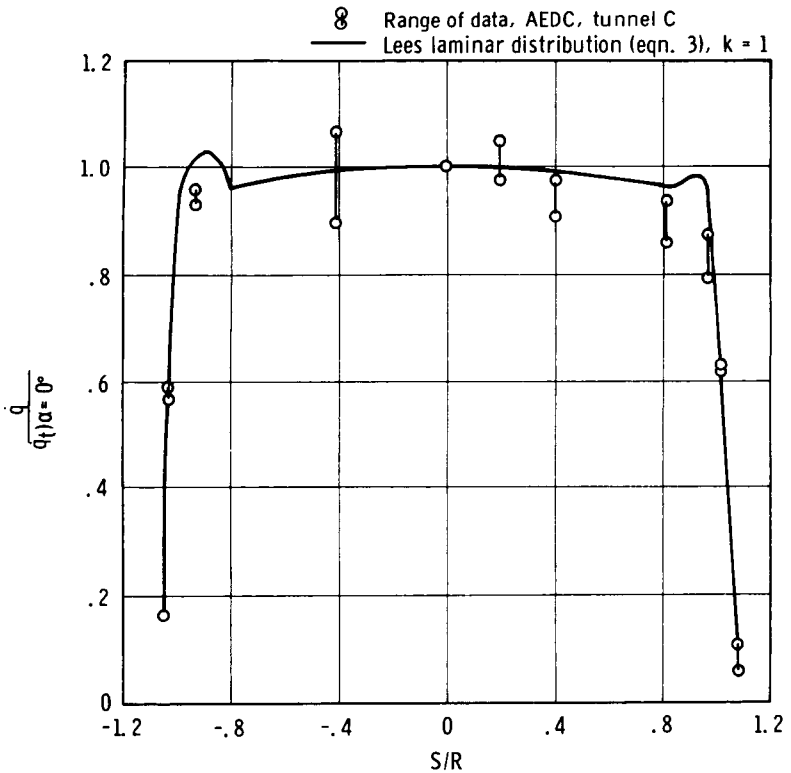

(a)α= 0°.

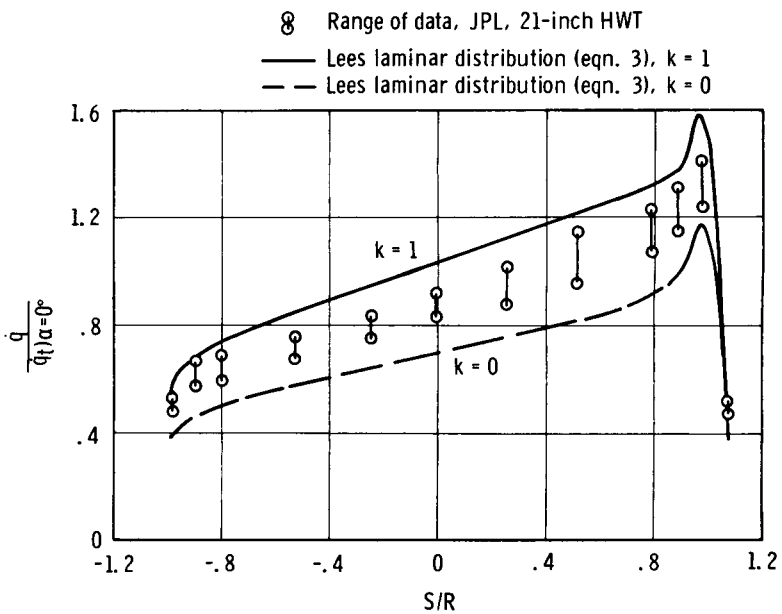

(b)α= 20°.

Figure 8. - Heat transfer rate distribution for the pitch plane of the spherical heat shield.

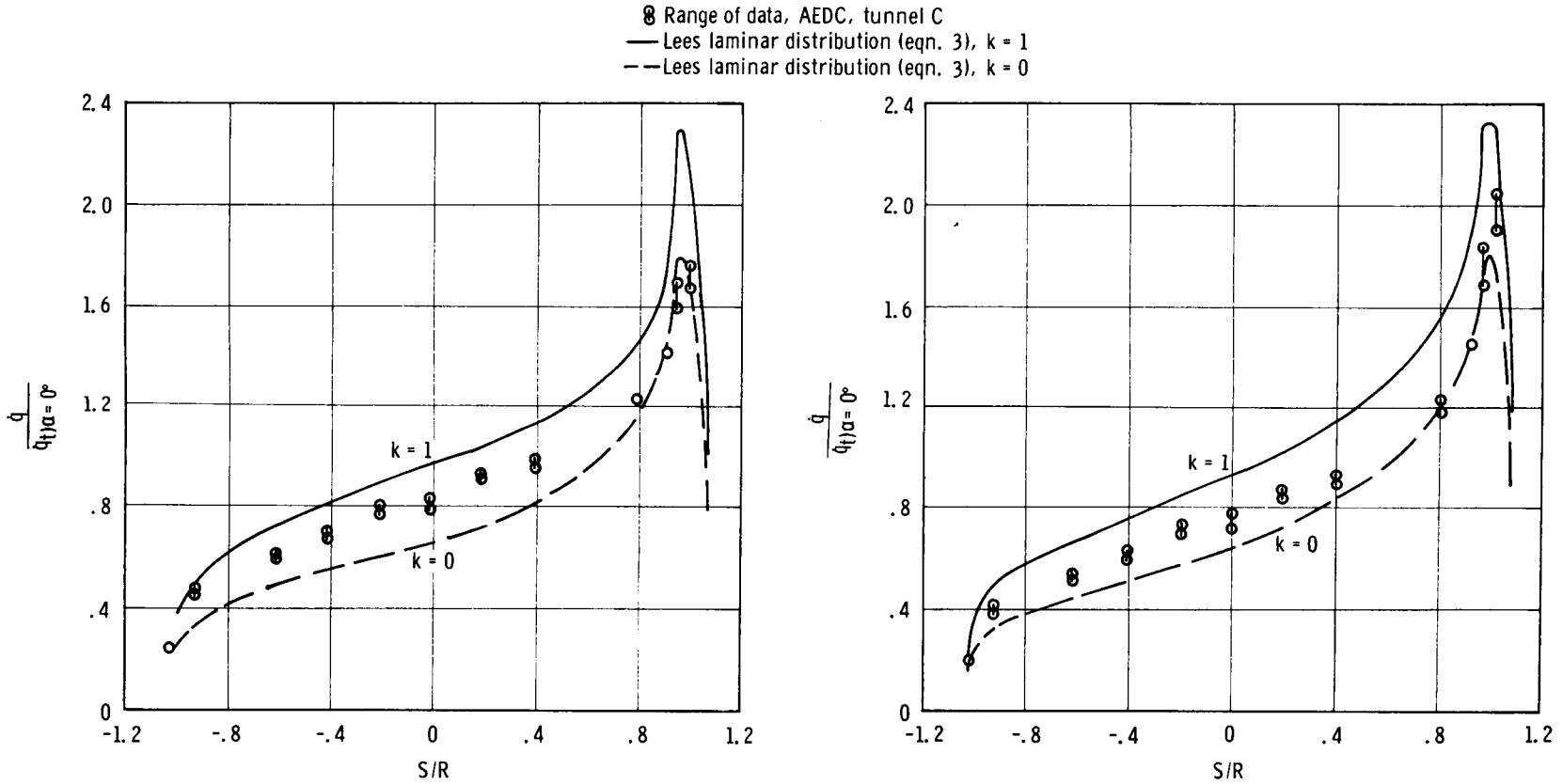

(c)α = 28°.

(d)α = 33°.

Figure 8. - Concluded.

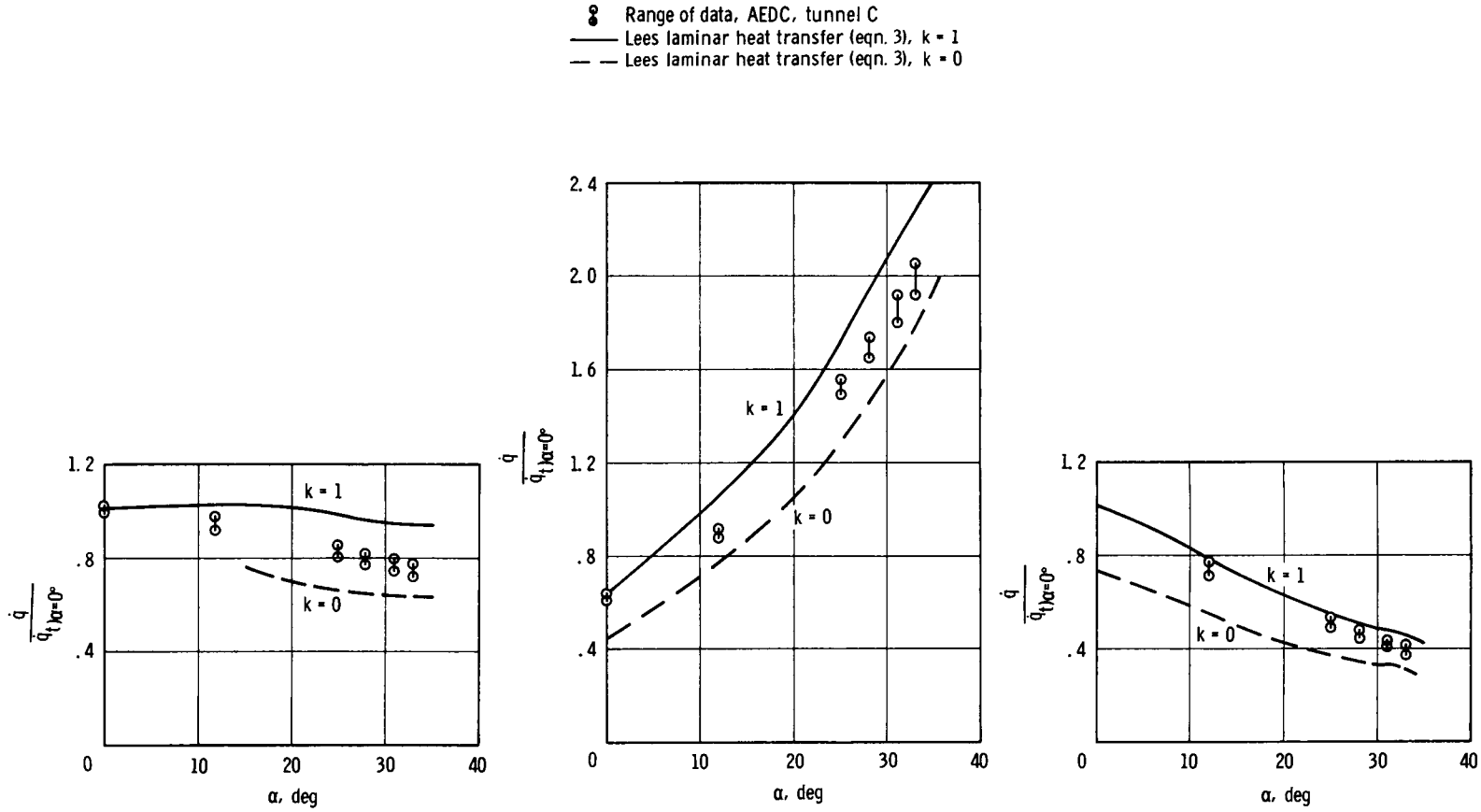

(a) S/R = 0, λ = 0°.

(b) S/R = 1.02, λ = 0°.

(c) S/R = .93, λ = 180°.

Figure 9. - Forebody heat transfer rate as a function of the angle of attack.

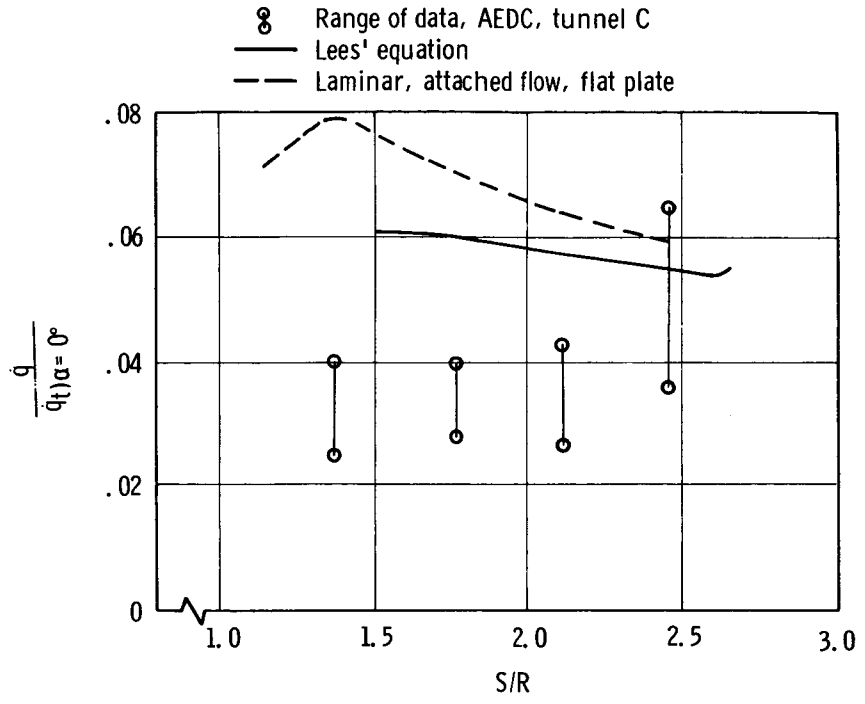

(a) $\alpha = 0°$.

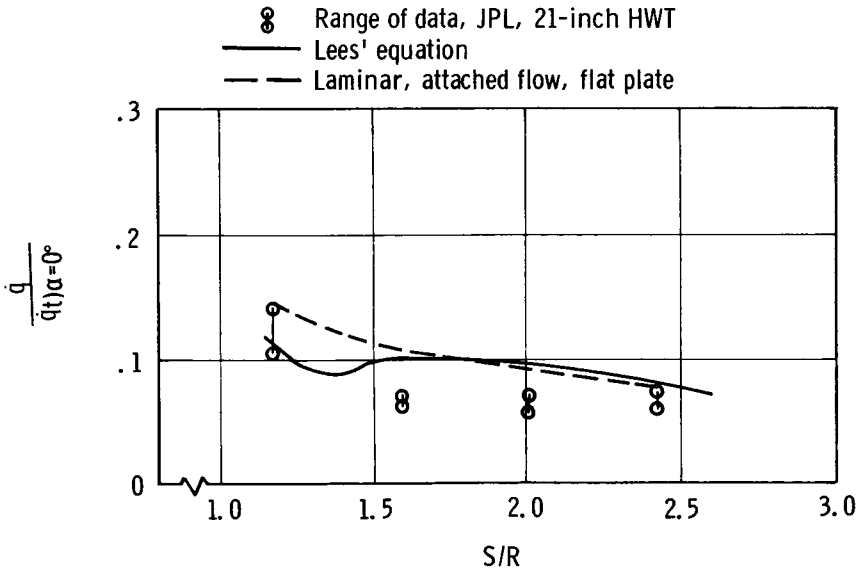

(b) $\alpha = 20°$.

Figure 10. - Heating rate distribution along the windward-most conical generator.

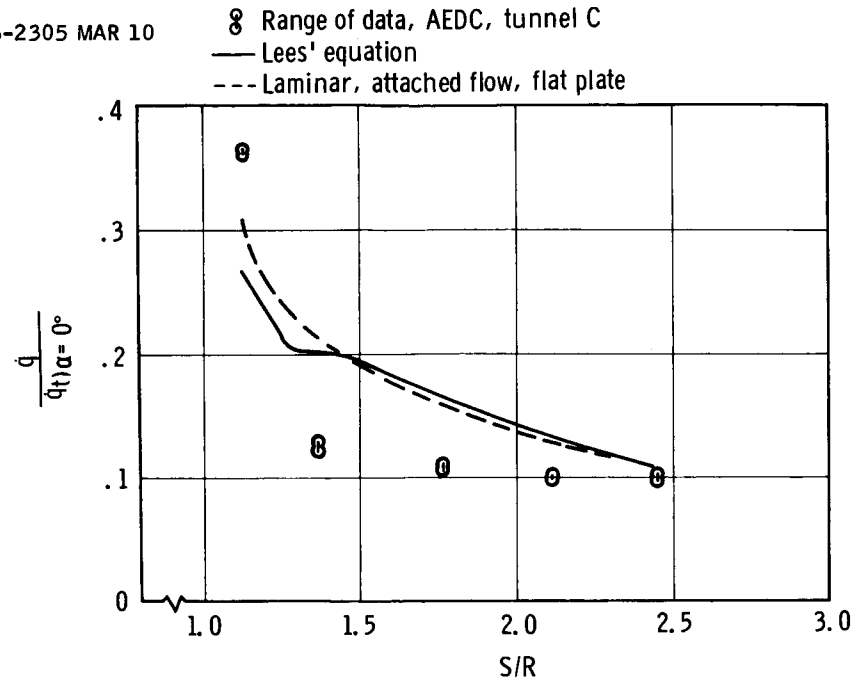

(c) = 28°.

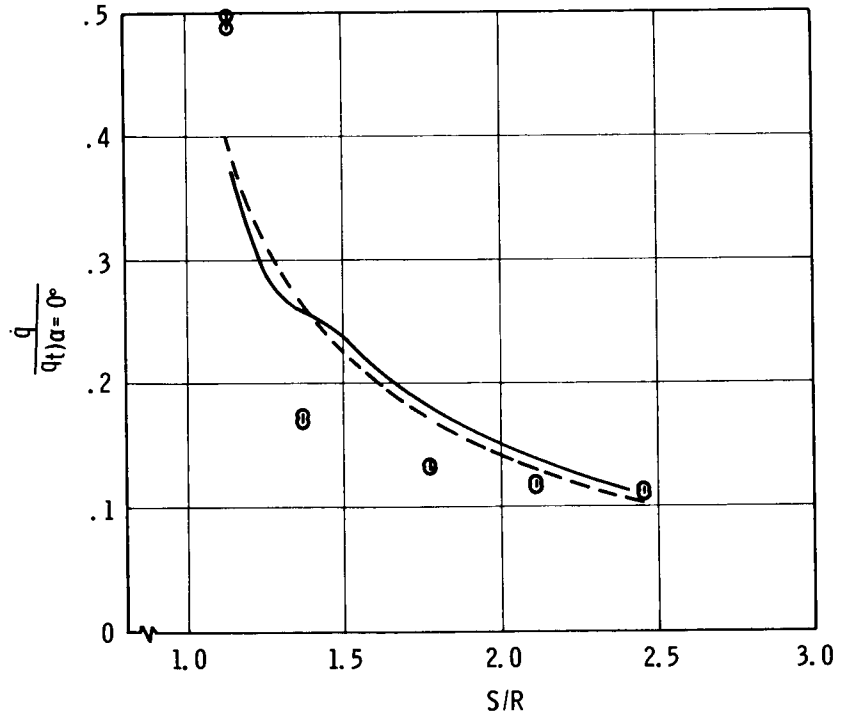

(d) = 33°.

Figure 10. - Concluded.

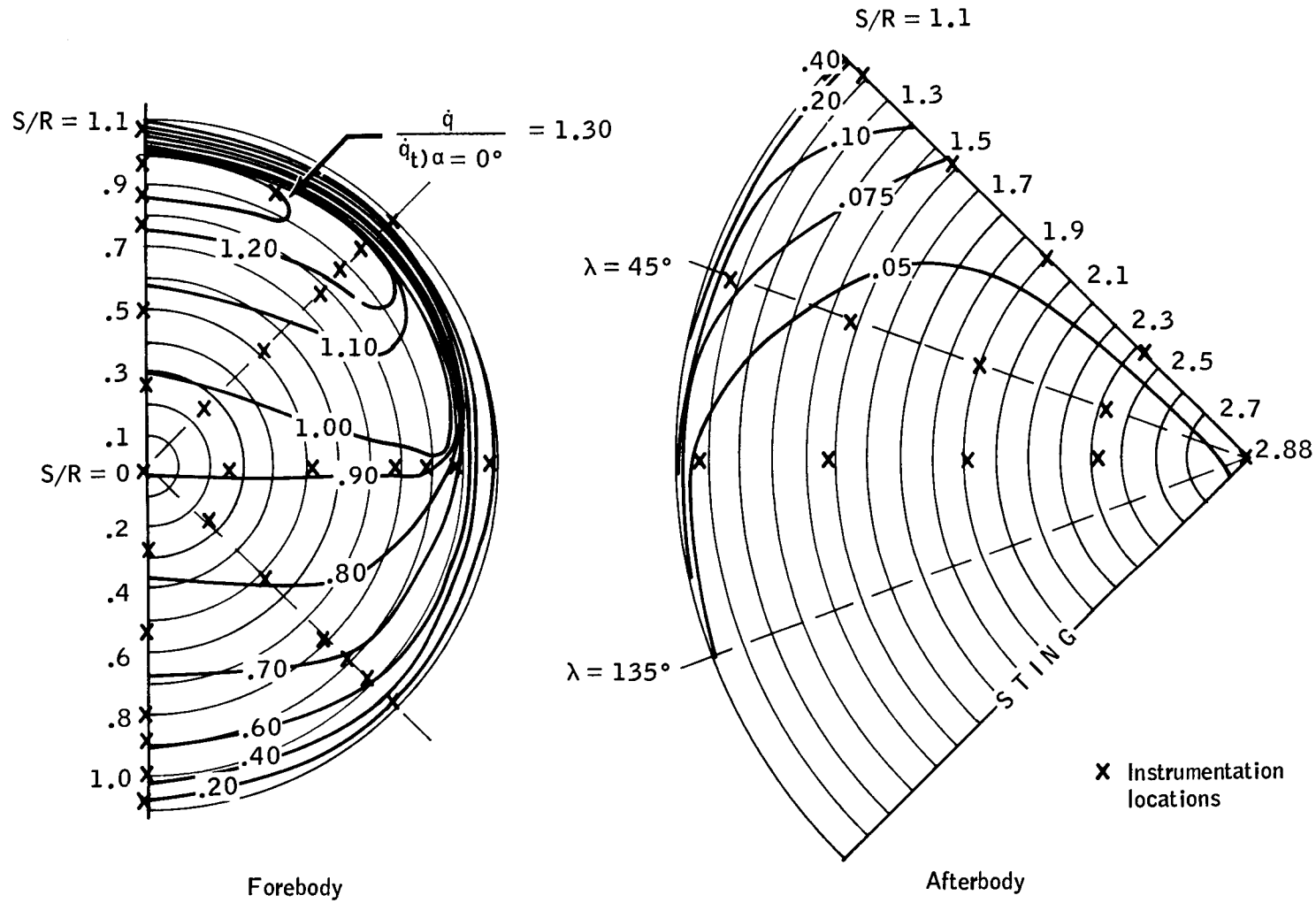

(a) $\alpha = 20°$.

Figure 11. - Hypersonic, laminar heat-transfer distribution for entire reentry configuration.

NASA-S-66-2297 MAR 10

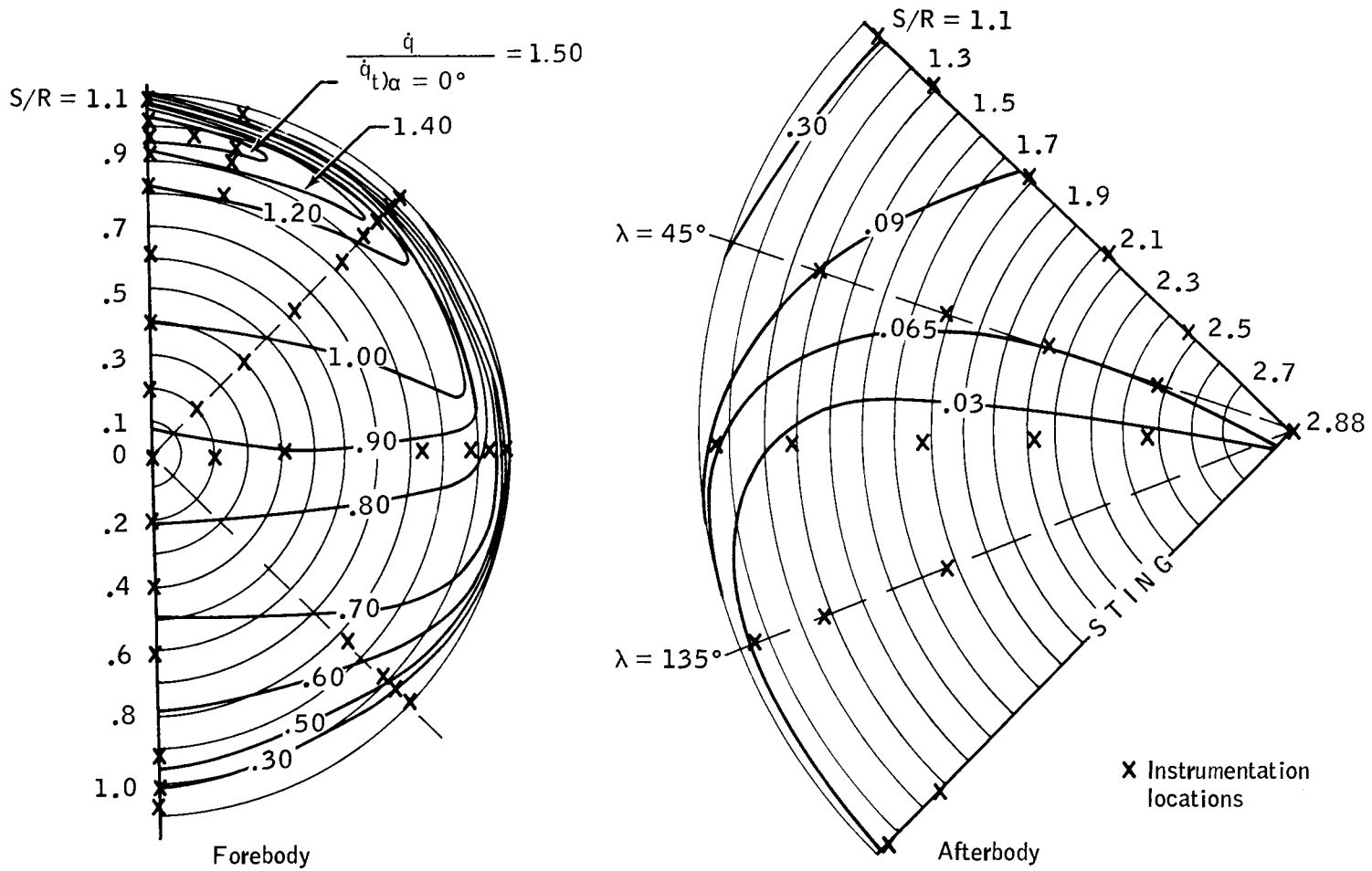

(b) $\alpha = 25°$

Figure 11. - Continued.

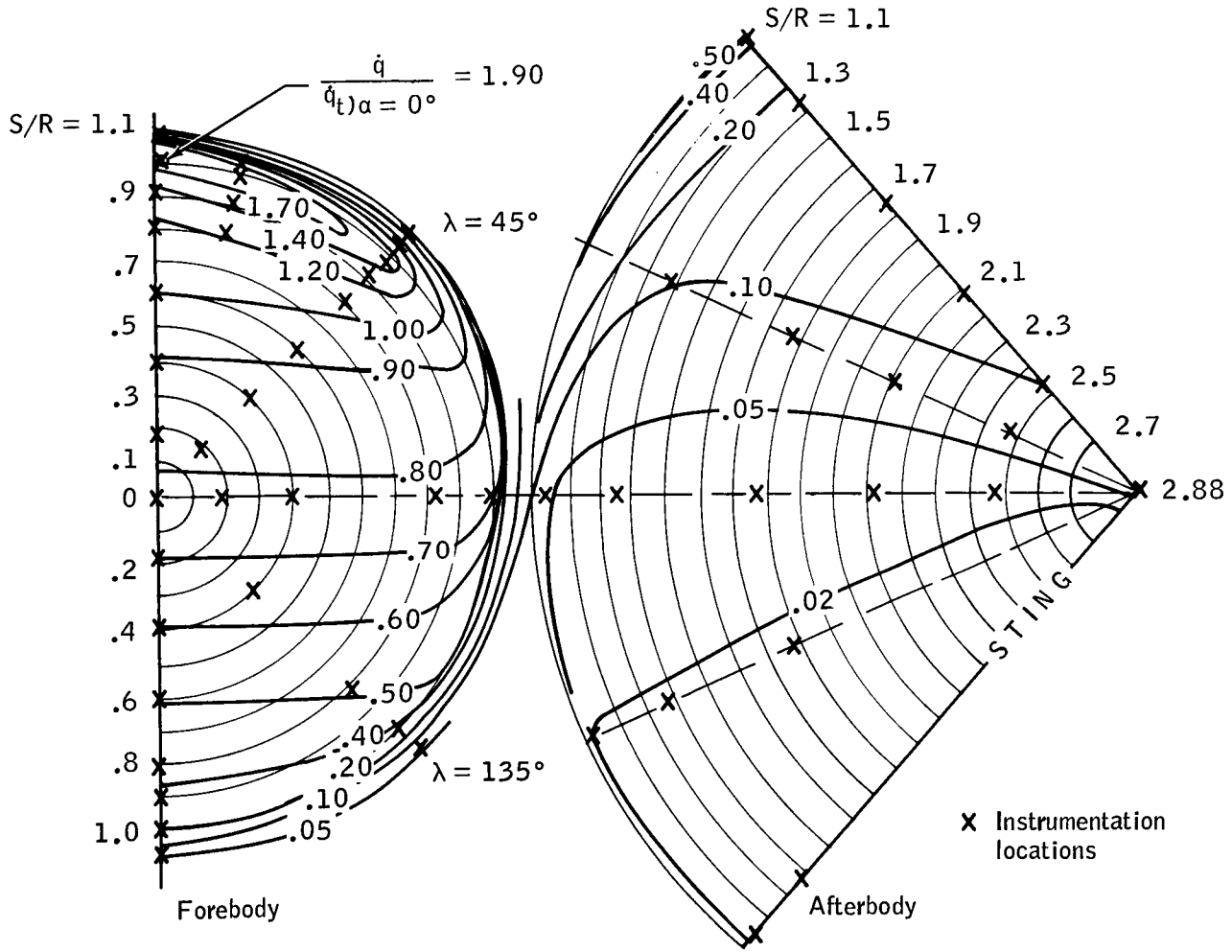

(c) α = 33°

Figure 11. - Concluded.

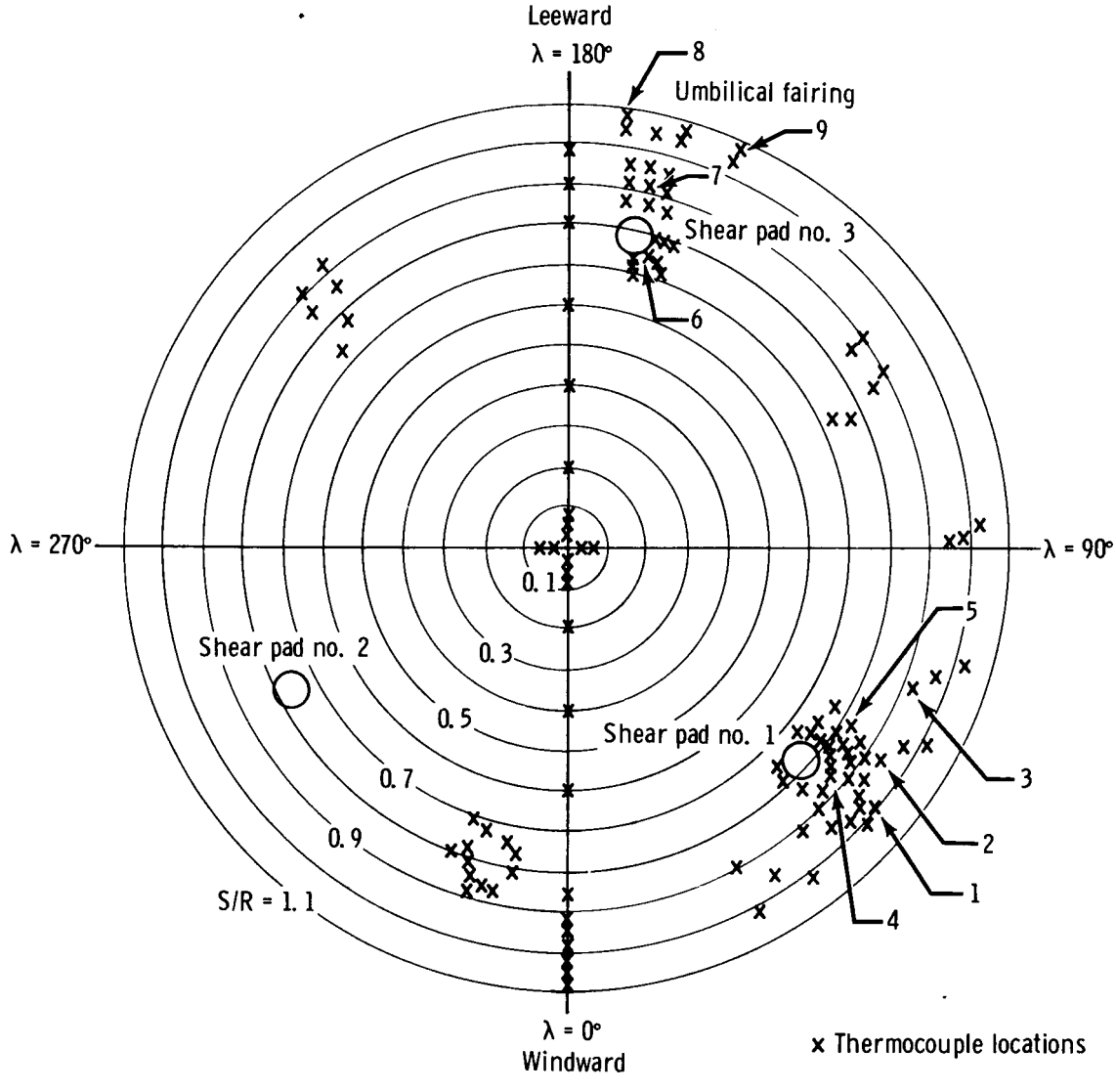

(a) Forebody

Figure 12. - Instrumentation locations and nomenclature for the cavities and proturbance model.

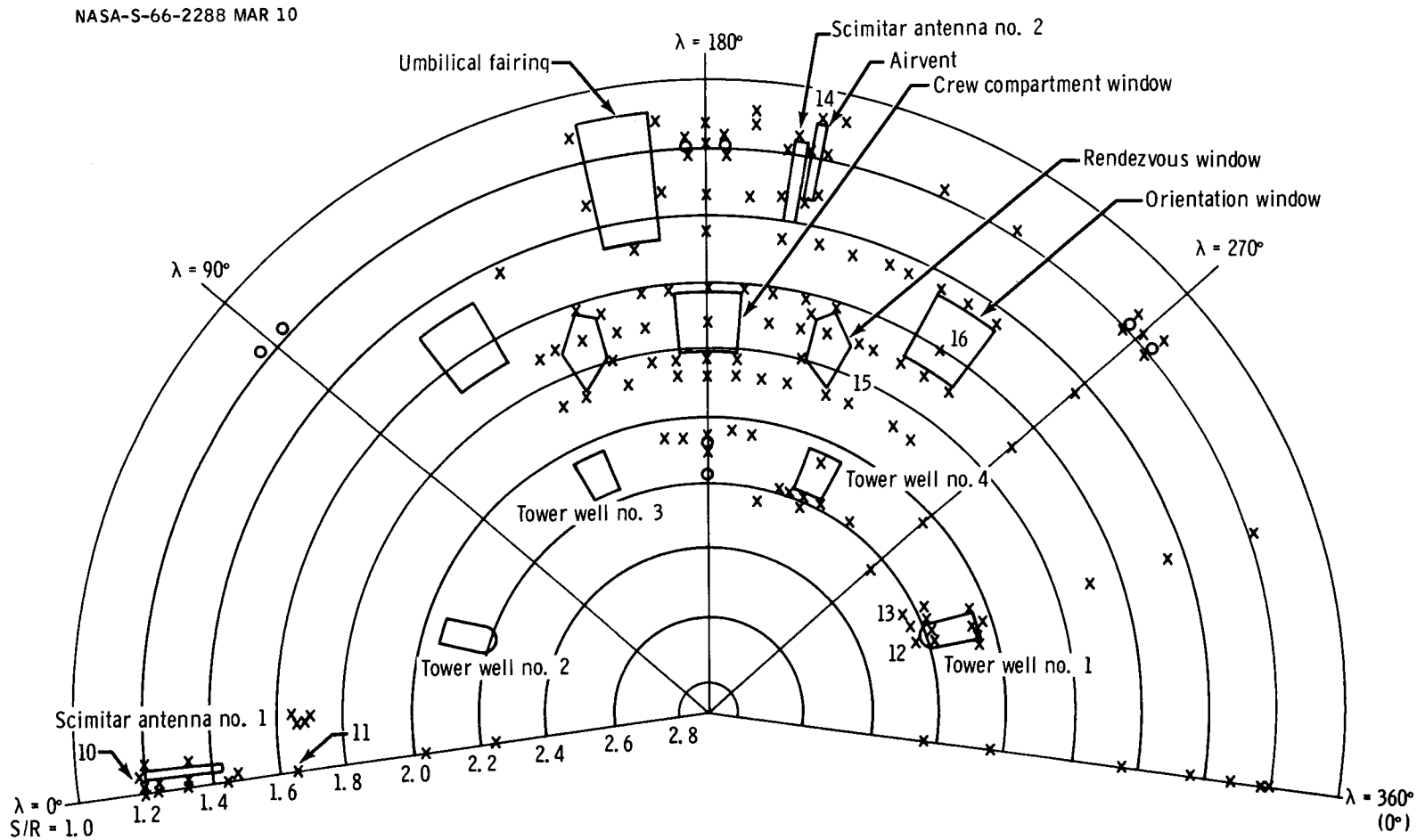

(b) Afterbody

Figure 12. - Concluded.

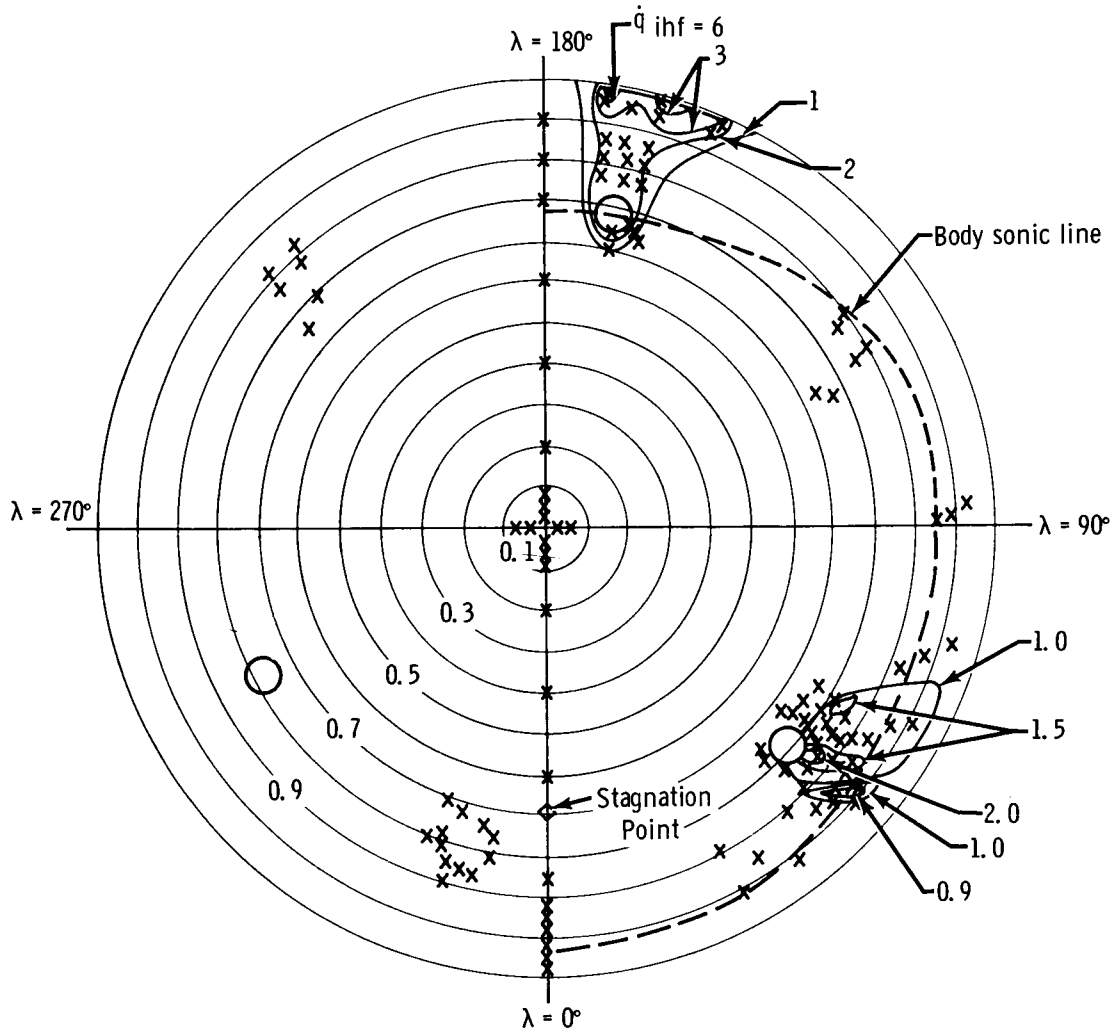

(a) $\alpha = 22°$, $M_\infty = 10.14$, $Re_D = 1.375$

Figure 13. - Interference heating distributions over the forebody.

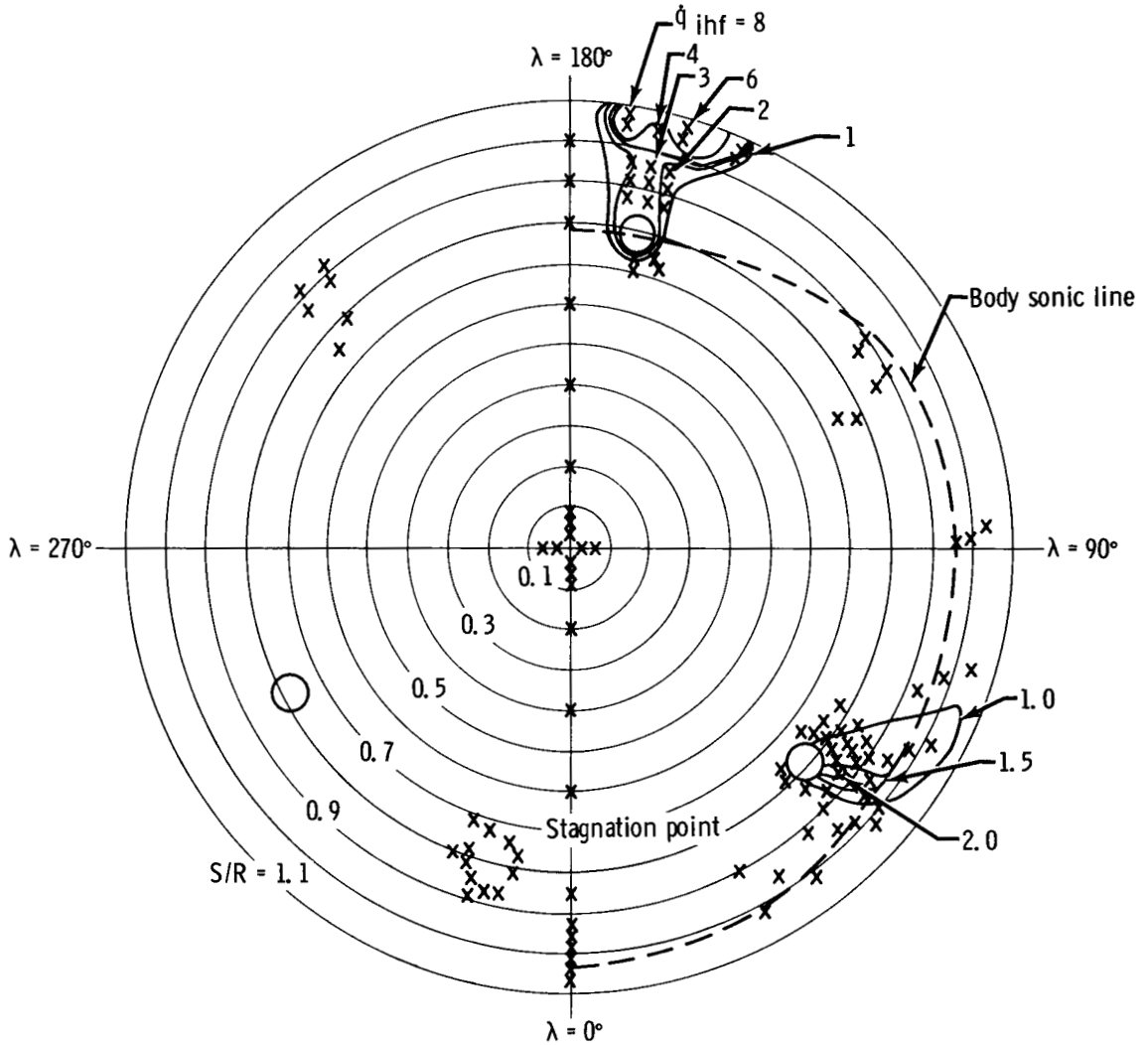

(b) $\alpha = 22°$, $M_\infty = 10.19$, $Re_D = 2.56 \times 10^6$.

Figure 13. - Continued.

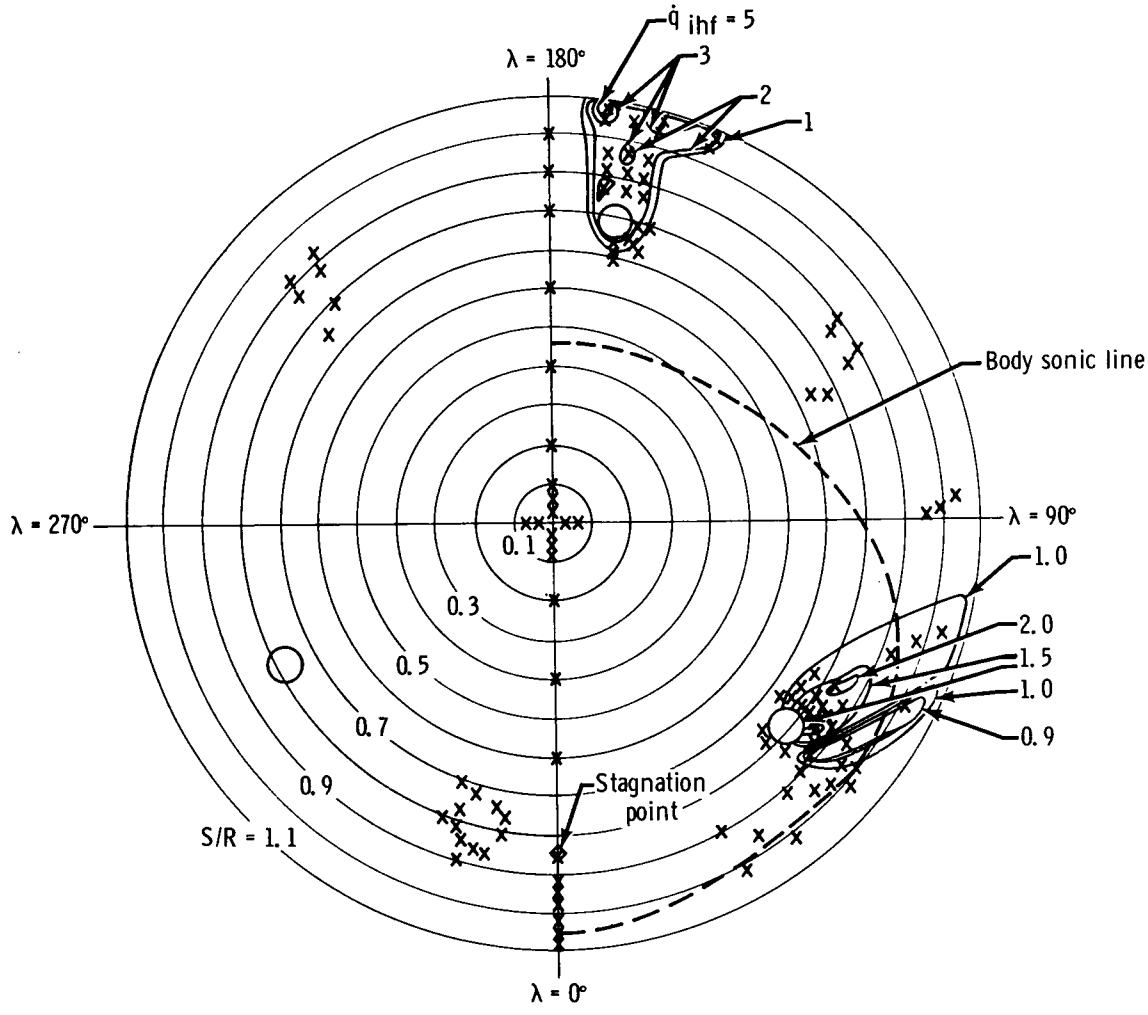

(c) $\alpha = 33°$, $M_\infty = 10.14$, $Re_D = 1.37 \times 10^6$.

Figure 13. - Continued.

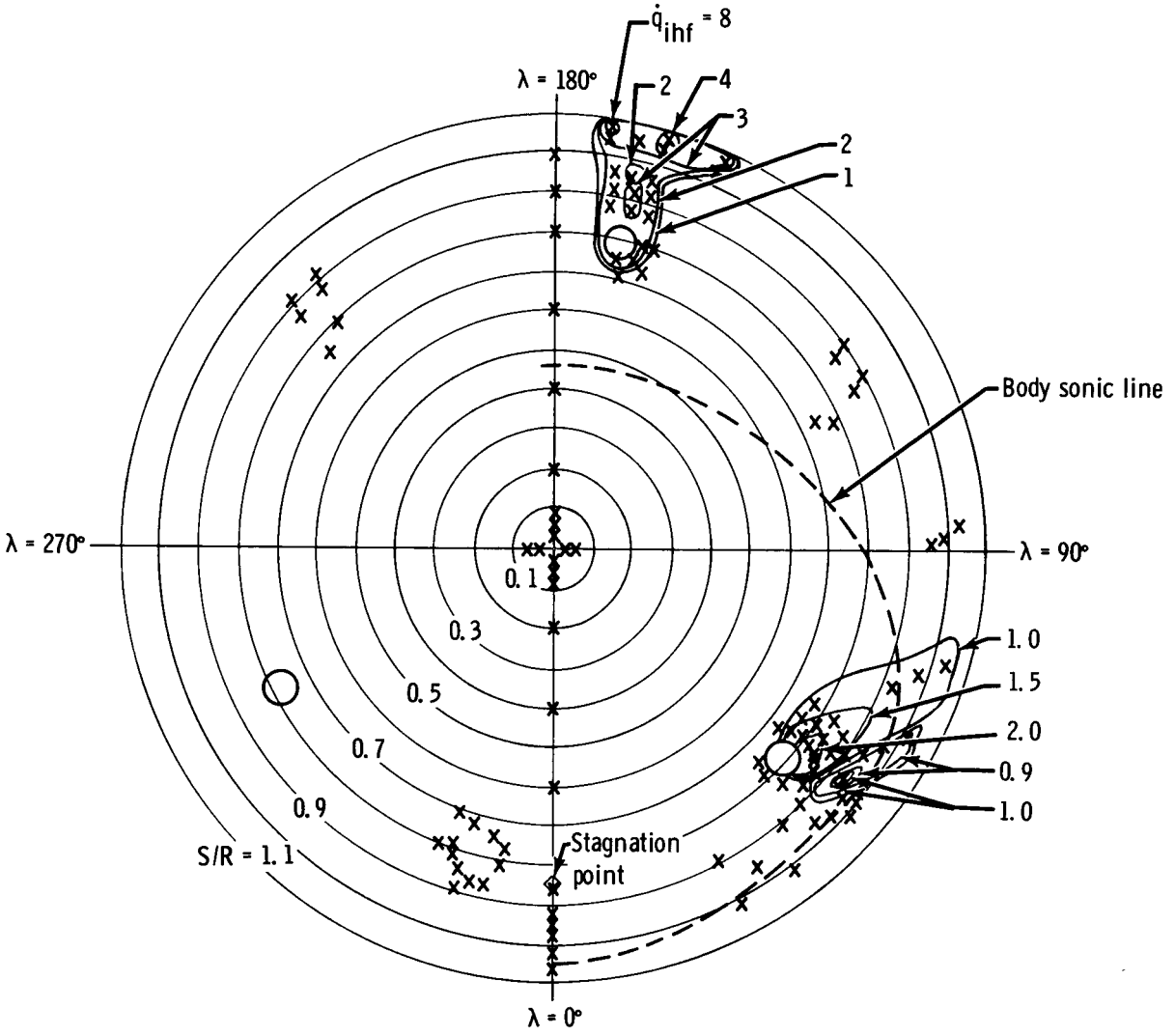

(d) $\alpha = 33°$, $M_\infty = 10.19$, $Re_D = 2.56 \times 10^6$.

Figure 13. - Concluded.

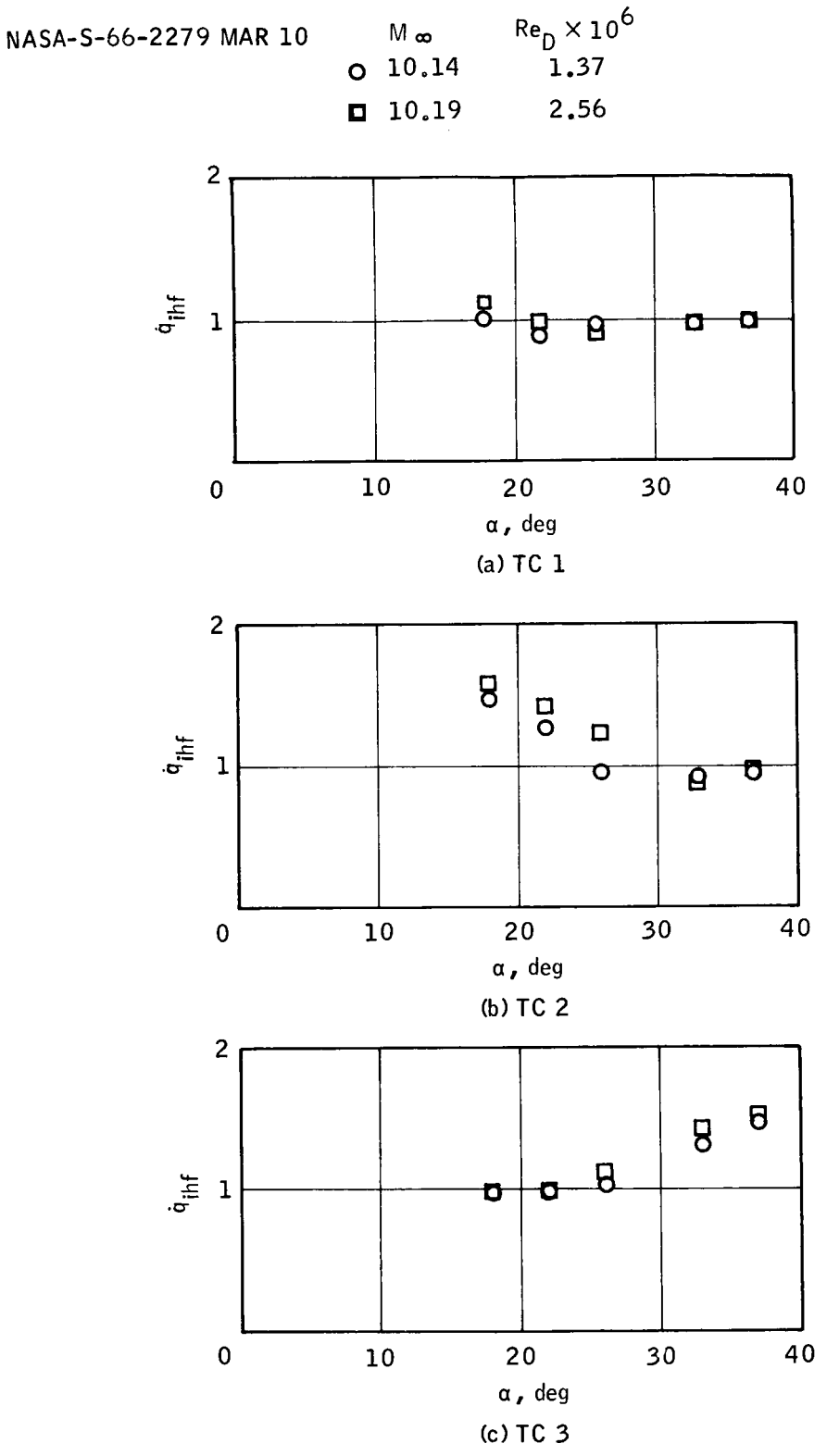

Figure 14. - Interference heating factors near shear pad no. 1.

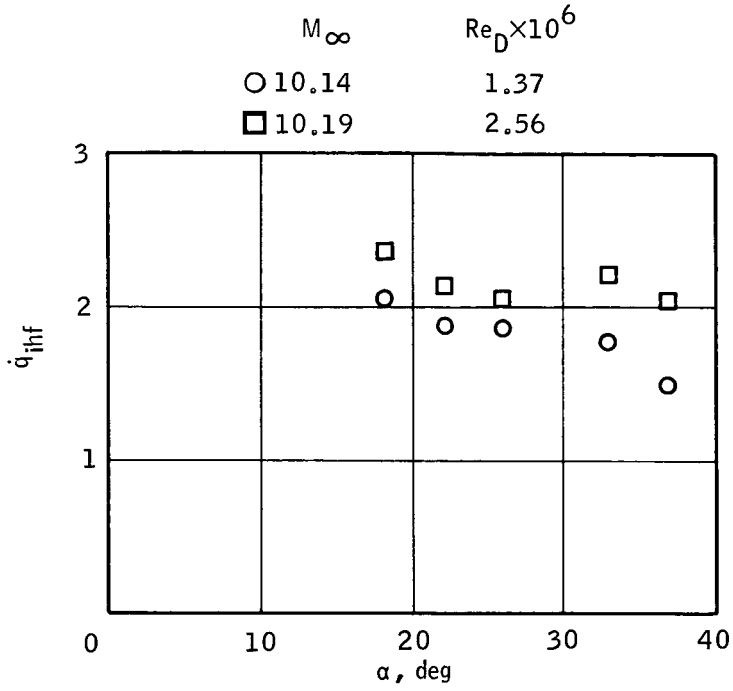

(d) TC 4

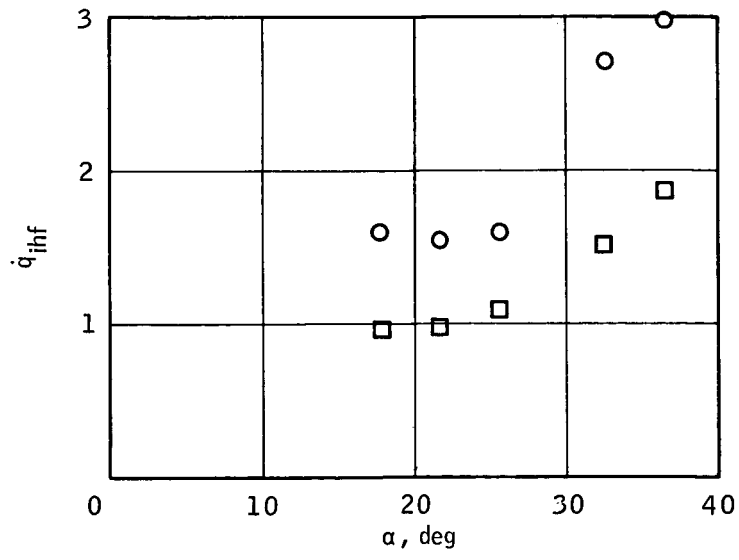

(e) TG 5

Figure 14. - Concluded.

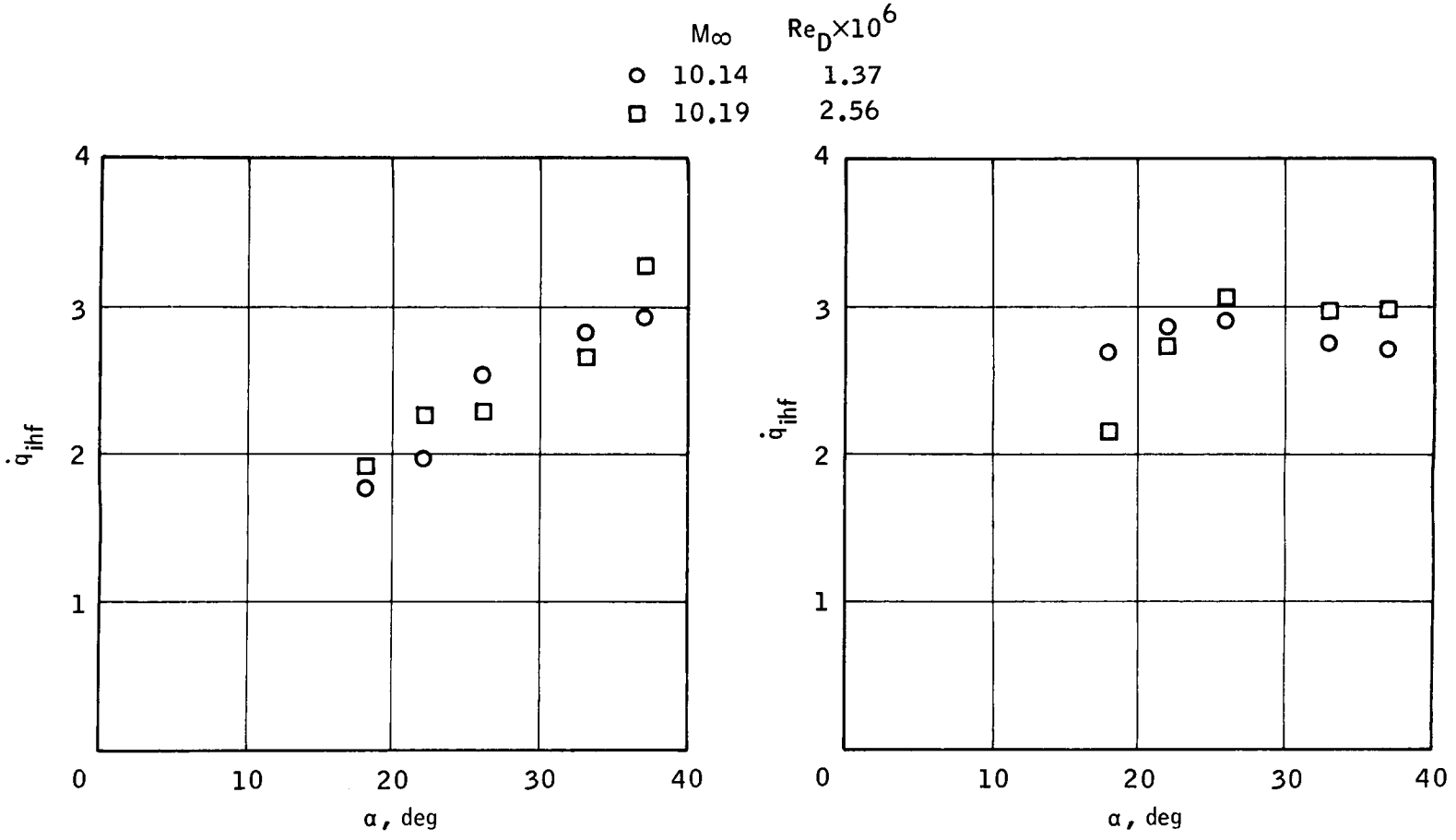

(a) TC 6 (b) TC 7

Figure 15. - Interference heating factors in the vicinity of shear pad no. 3 and the umbilical fairing.

NASA-S-66-2281 MAR 10

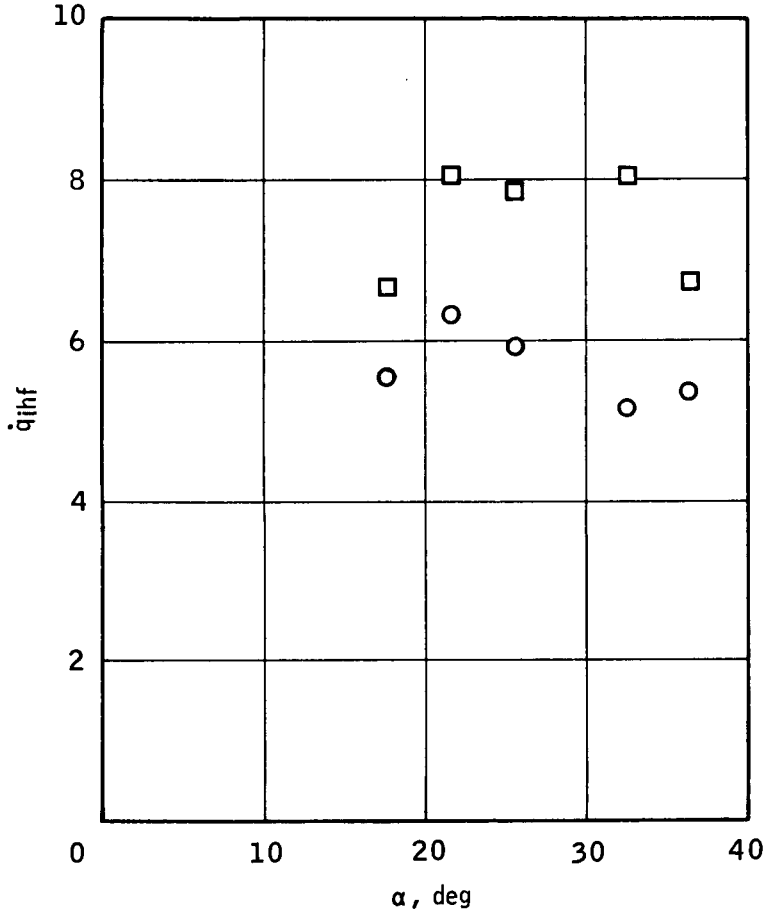

(c) TC 8

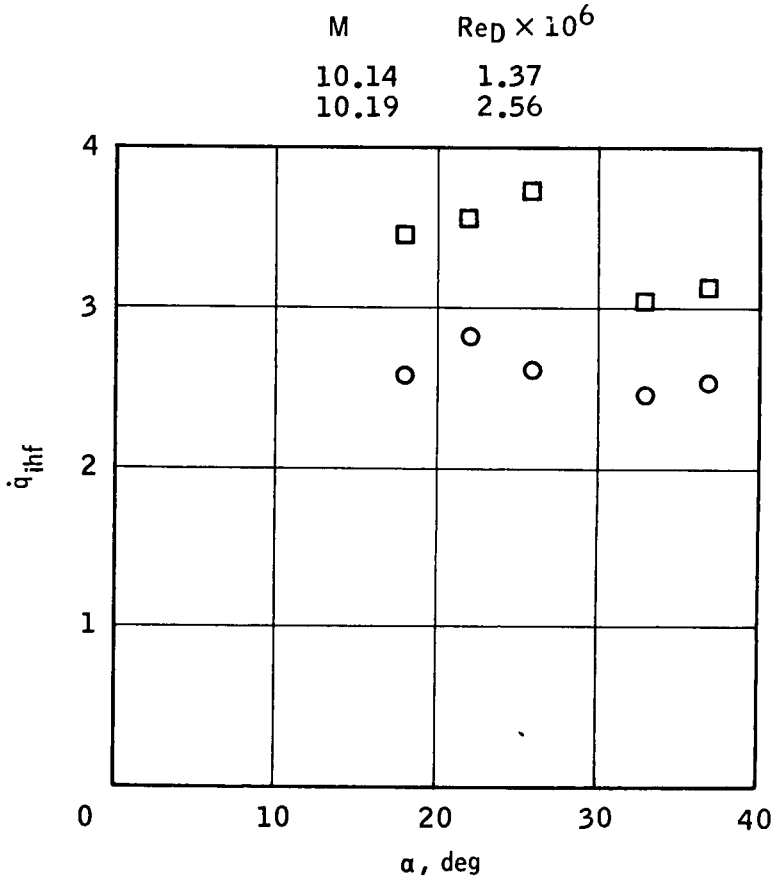

(d) TC 9

Figure 15. - Concluded.

NASA-S-66-2285 MAR 10

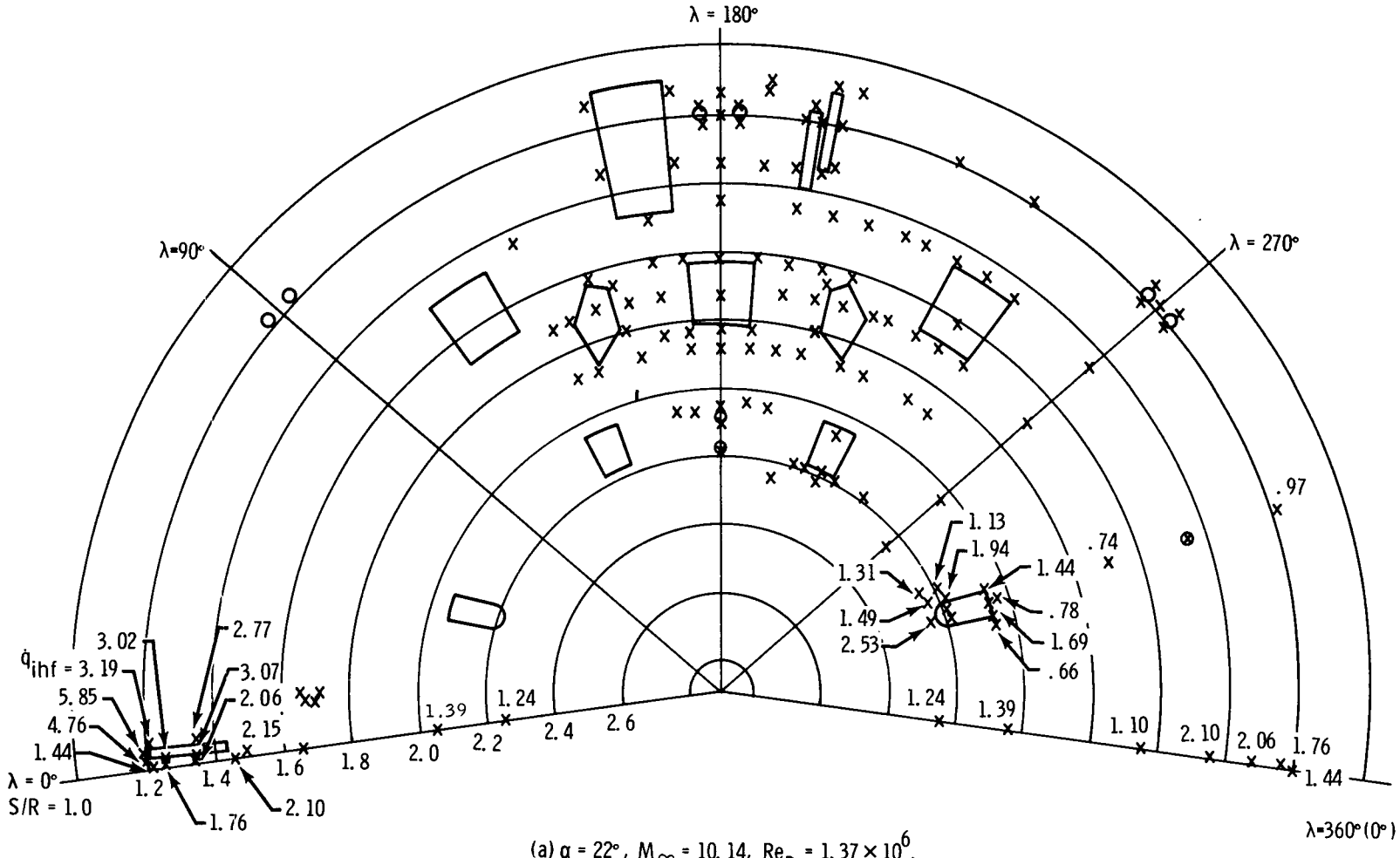

(a) $\alpha = 22°$, $M_\infty = 10.14$, $Re_D = 1.37 \times 10^6$.

Figure 16. - Interference heating factors on the windward afterbody.

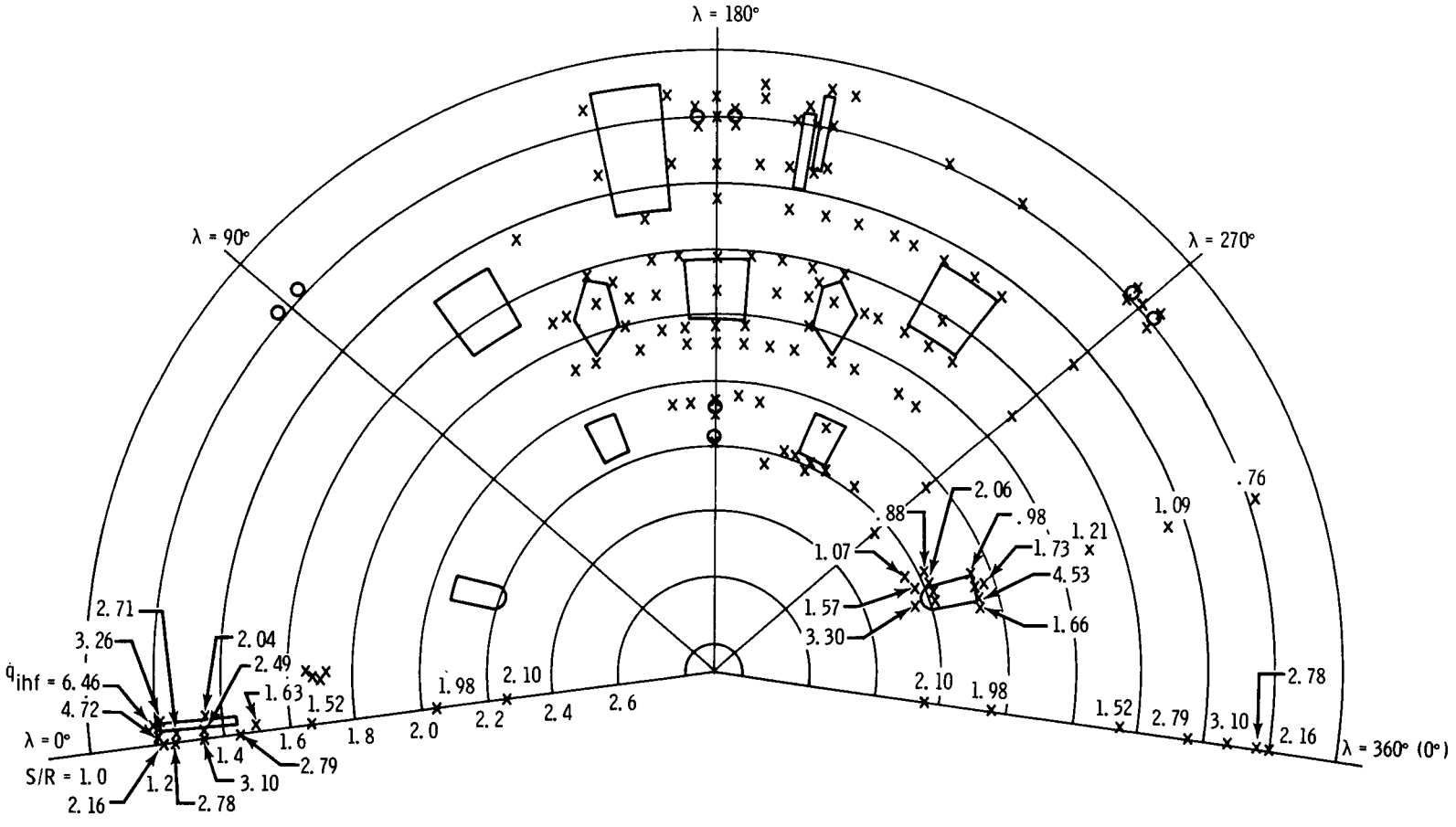

(b) $\alpha = 22°$, $M_\infty = 10.19$, $Re_D = 2.56 \times 10^6$.

Figure 16. - Continued.

NASA-S-66-2303 MAR 10

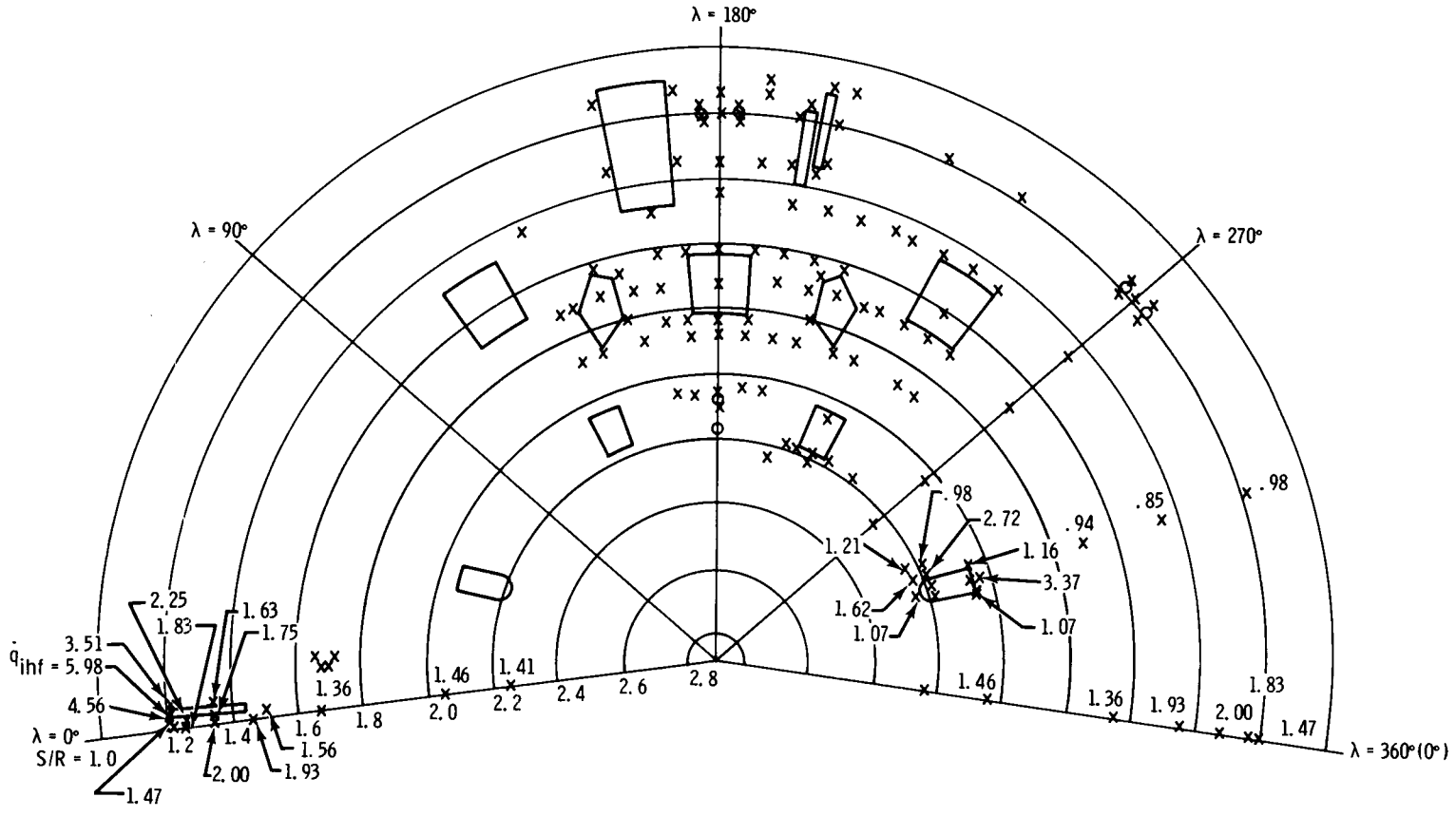

(c) $\alpha = 33°$, $M_\infty = 10.14$, $Re_D = 1.37 \times 10^6$.

Figure 16. - Continued.

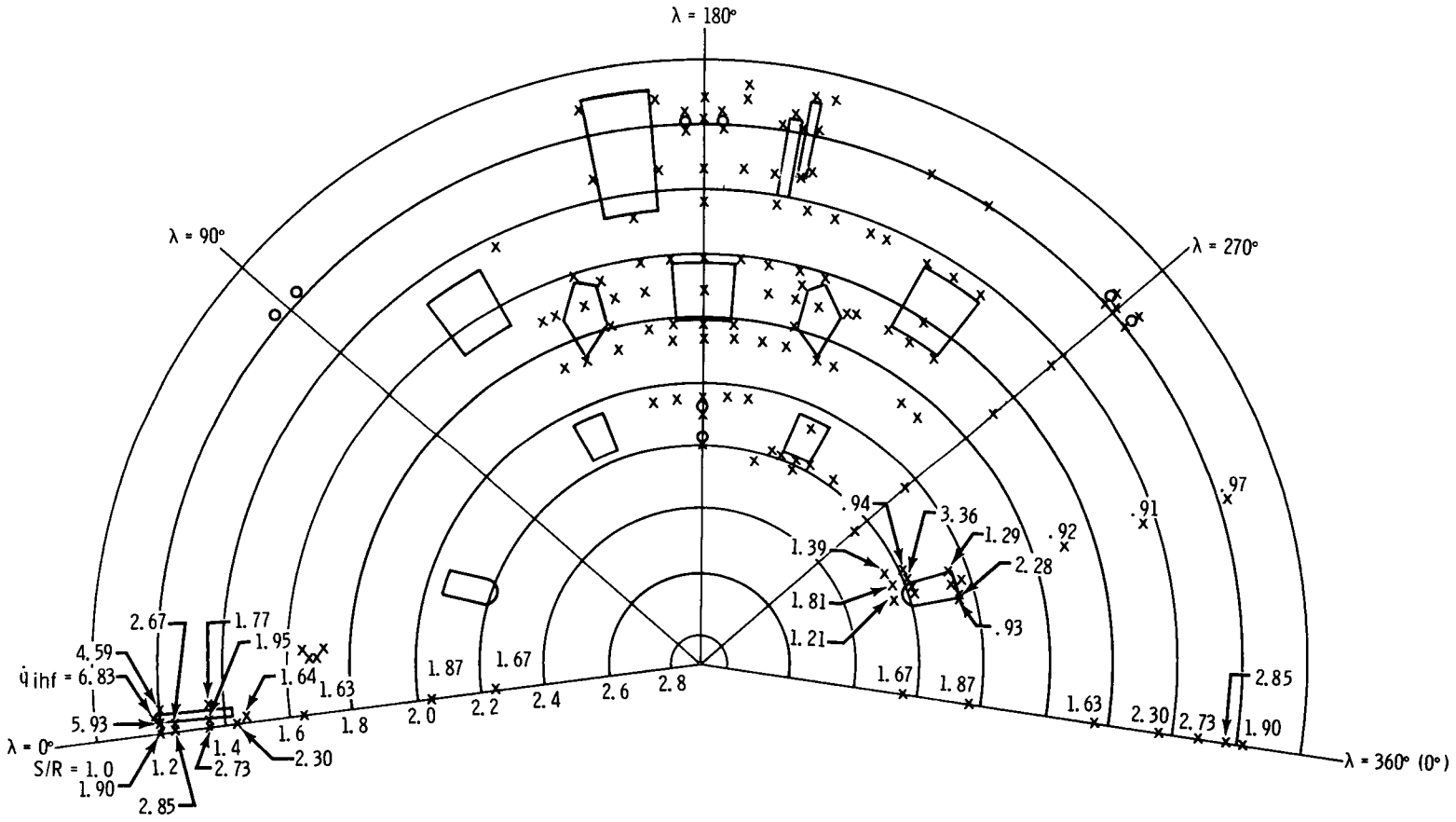

(d) $\alpha = 33°, M_\infty = 10.19, Re_D = 2.56 \times 10^6$.

Figure 16. - Concluded.

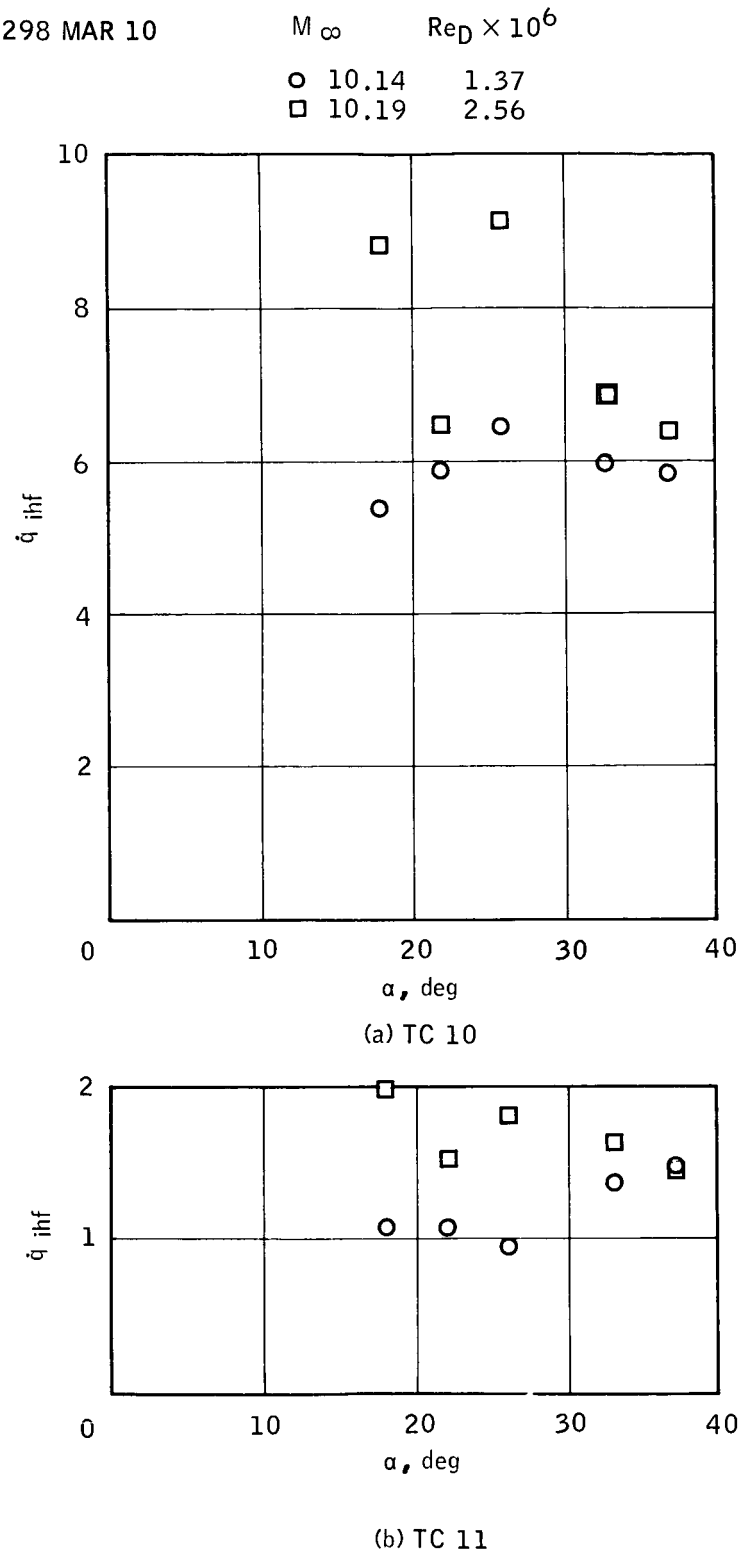

Figure 17. - Interference heating factors in the vicinity of the windward antenna housing.

NASA-S-66-2299 MAR 10

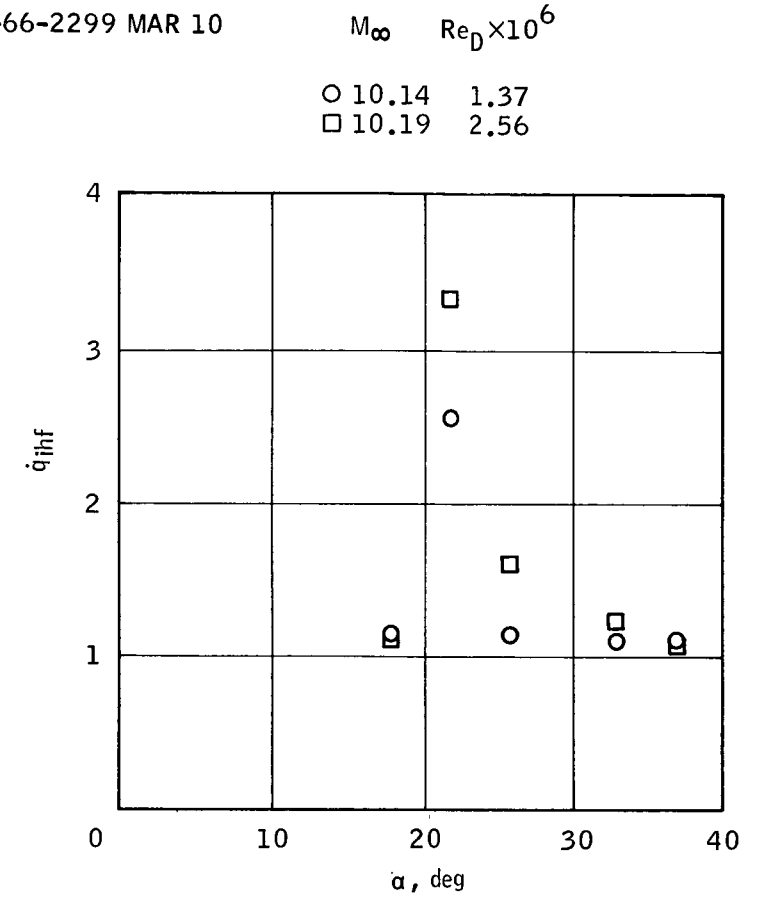

(a) TC 12

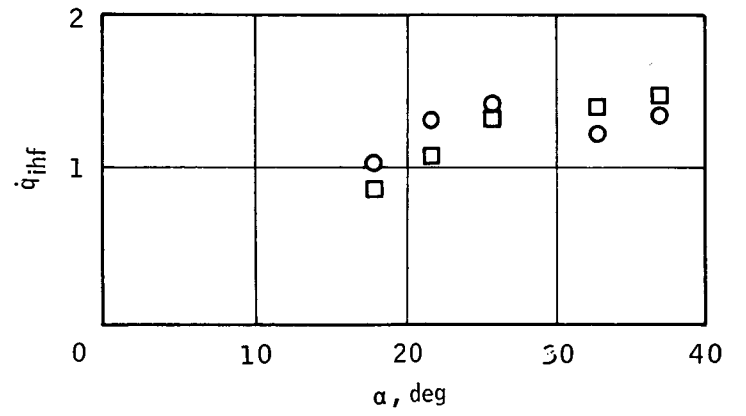

(b) TC 13

Figure 18. - Interference heating factors in the vicinity of tower well no. 1.

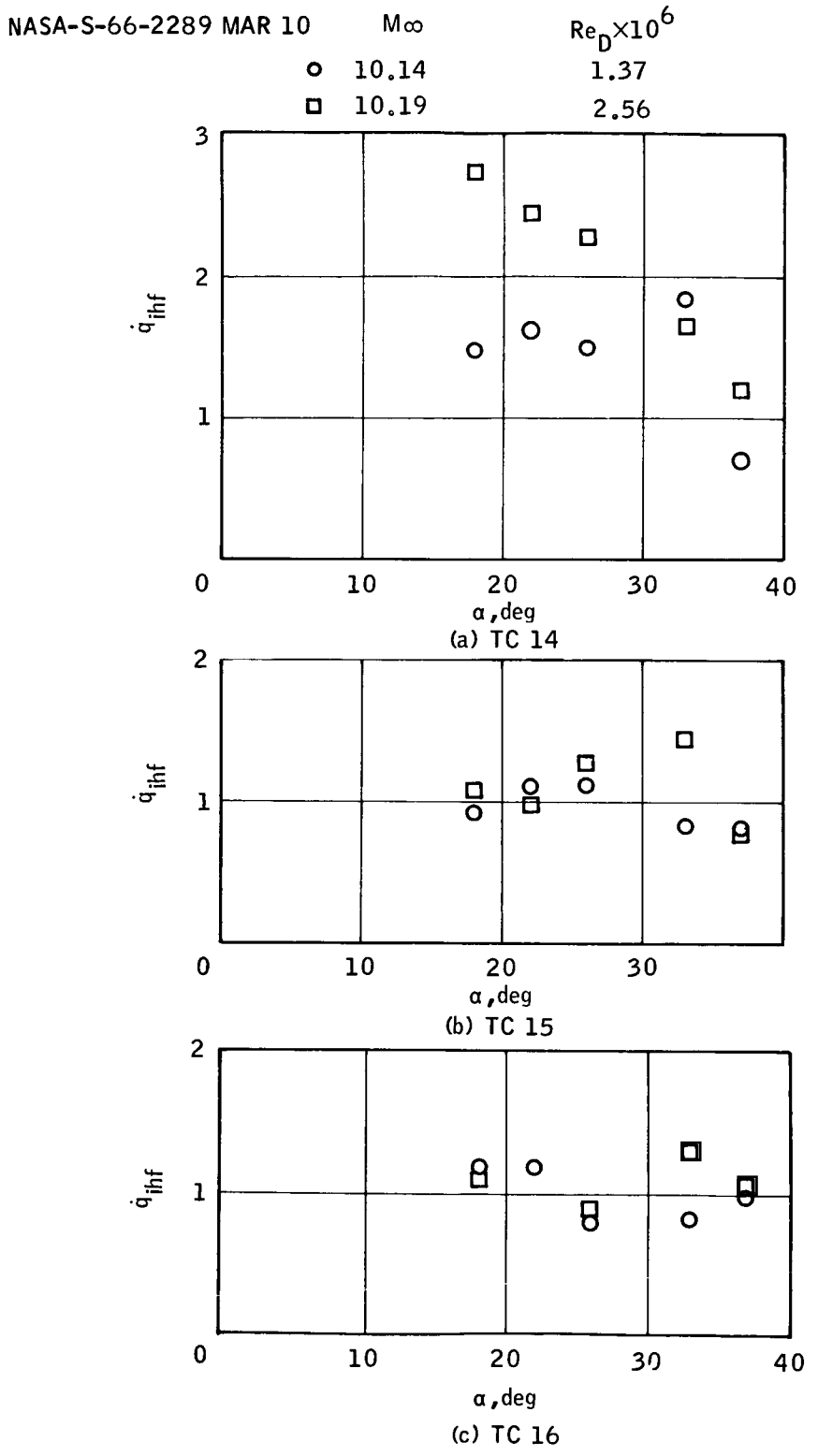

Figure 19. - Interference heating factors on the leeward afterbody.